JARS Journal of Applied Remote Sensing

REVIEW

Mineral classification on Martian surface using CRISM hyperspectral data: a survey

Priyanka Kumari,[a,*] **Sampriti Soor**,[b] **Amba Shetty**,[a] **and Shashidhar G. Koolagudi**[c]

[a]National Institute of Technology Karnataka, Department of Water Resources and Ocean Engineering, Mangalore, Karnataka, India

[b]Kalinga Institute of Industrial Technology, School of Computer Engineering, Bhubaneswar, Odisha, India

[c]National Institute of Technology Karnataka, Department of Computer Science and Engineering, Mangalore, Karnataka, India

ABSTRACT. The compact Reconnaissance Imaging Spectrometer for Mars (CRISM) has significantly advanced our understanding of the mineralogy of Mars. With its enhanced spectral and spatial resolution, CRISM has enabled the identification and characterization of various minerals on the Martian surface, providing valuable insights into Mars' past climate and geologic history, as well as the evolution of the planet's atmosphere and climate. We present a comprehensive review of mineral identification on Mars using CRISM data. We discuss the data description, pre-processing techniques, different spectrum libraries, geological characteristics used for mineral identification, challenges, and methodologies used for mineral classification, such as learning models, probabilistic methods, and neural networks. We highlight major findings of minerals on the Martian surface and discuss validation techniques. We conclude with a discussion of further research to address the existing gaps and challenges in this field. Overall, we provide a general understanding of mineral classification using CRISM data and could serve as a helpful resource for researchers and scientists interested in planetary remote sensing and mineral identification on the Martian surface.

 [DOI: 10.1117/1.JRS.17.041501]

Keywords: CRISM data; Martian surface; mineral identification; classification models; pre-processing; validation

Paper 230300V received Jun. 22, 2023; revised Oct. 2, 2023; accepted Oct. 23, 2023; published Nov. 11, 2023.

1 Introduction

The compact Reconnaissance Imaging Spectrometer for Mars (CRISM) is a highly effective tool that has significantly advanced researchers' understanding of the mineralogy of Mars. CRISM, equipped with enhanced spectral and spatial capabilities, has successfully obtained a multitude of consecutive images from significant Martian regions, including volcanic areas, precipitous cliffs, and sedimentary deposits, thereby improving our understanding of the planet's surface. CRISM has enabled the identification and characterization of various minerals, notably, the detection of phyllosilicates including kaolinite, hydrated silica, and different types of smectites.[1] This detection is of particular significance as these minerals are typically formed in the presence of liquid water. Apart from phyllosilicates, CRISM has also detected different mafic minerals, carbonates, and sulfates.[2–4] The identification and mapping of these minerals provide valuable insights into

*Address all correspondence to Priyanka Kumari, priyanka.187am004@nitk.edu.in

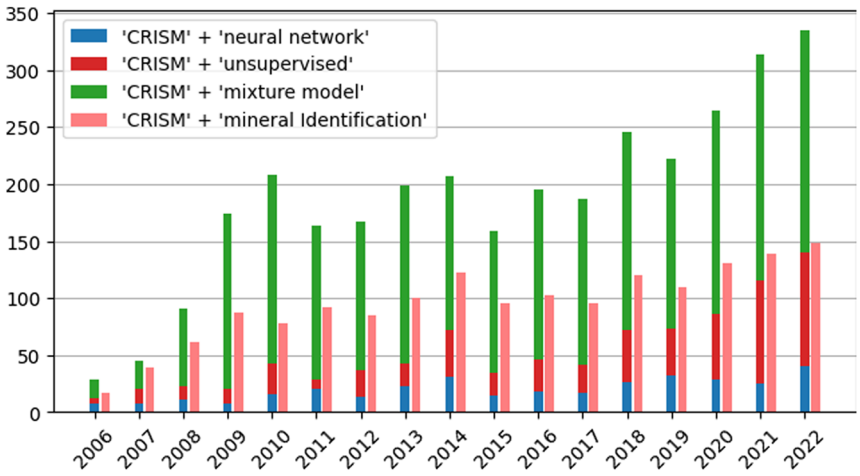

Fig. 1 Number of publications in the last decade based on the Google Scholar and Scopus research publication database.

Mars' past climate and geologic history, as well as the geologic processes that have shaped the Martian surface and the evolution of the planet's atmosphere and climate.

During its Primary Science Phase operation, which spanned from November 2006 to October 2010, Mars Reconnaissance Orbiter (MRO) aimed to achieve several scientific objectives, such as studying seasonal variations in the Martian atmosphere and surface, detecting evidence of historical water presence and its effects on the Martian surface, and mapping and characterizing the geology, stratigraphy, and identifying the composition of surface deposits[5] MRO's extended phase mission aims to determine the feasibility of potential future landing sites, assess Mars rover traversal, and provide a data relay service from ground missions back to Earth. Overall, MRO has provided a wealth of scientific data that will continue to be analyzed and studied for years to come.[5,6]

Figure 1 shows a systematic review of the literature on mineral identification on the Martian surface published in the last 15 years since the launch of the MRO mission. To obtain the number of papers published during this period, relevant keywords, such as "mineral identification," "unsupervised," "neural network," and "mixture models," along with the common keyword "CRISM" were searched in Google Scholar and Scopus databases. The graph illustrates a consistent increase in the number of publications focusing on the utilization of CRISM data for mineral classification on the Martian surface over the last decade. Notably, the integration of a neural network and unsupervised approach with CRISM data is one of the predominant interests for Martian data researchers and experts currently. Therefore, a systematic review paper on this topic can provide a comprehensive and up-to-date understanding of the advancements in mineral identification using CRISM data. This can be useful for future research and development in this field. It can also identify the existing gaps and challenges as well as suggest potential solutions and future research directions.

The word cloud in Fig. 2, build upon the titles, keywords, and abstracts of the published literature in this field, provides a comprehensive overview of mineral classification using CRISM data. It sheds light on various aspects, such as objectives, methodologies, study areas, and identified minerals. Bigger fonts indicate more frequently researched concepts. Notably, research spans noise correction methods, such as "volcano-scan" and "discrete ordinate radiative transfer (DISORT) model," alongside preprocessing techniques, such as "smoothing" to mitigate persistent spectral irregularities post-noise correction, and "continuum removal" to counteract global curvature changes in the captured spectra. Specific study regions, such as "Jezero Crater" and "Gale Crater," as potential landing sites for multiple Mars missions, garner significant attention, as do dominant Martian surface minerals, such as the "phyllosilicate group" and "mafic group," which aligns with the presumption of the presence of water on Mars' ancient environment. Unsupervised mineral classification methods, such as discovery through eigenbasis modeling of uninteresting data (DEMUD) and sequential maximum angle convex cone (SMACC), are highlighted, as are "summary products" and "browse products," pivotal for manual mineral

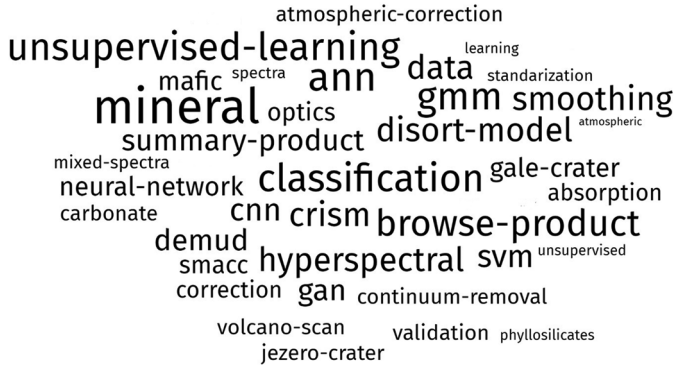

Fig. 2 Cloud tag of the titles, abstract, and keywords of the publications mentioned in Fig. 1, which are also covered in this review.

mapping in Martian imagery and also for result validation. Notably, the rising preference for different neural network models signifies a significant shift in recent research trends, underlining their efficacy in mineral identification. These various facets constitute the core focus of discussion in this comprehensive survey paper. Figure 3 provides a simplified illustration of the phases involved in mineral identification on the Martian surface, spanning data collection to results validation, serving as a visual aid to demonstrate the procedure's complexity.

This paper provides a comprehensive review of mineral identification on Mars using CRISM data, as well as an overview of the methods and techniques used for processing this remote sensing data. The paper is organized into sections that cover various aspects of the mineral identification process. Section 2 provides a data description, including the spectral and spatial resolution for both multispectral and hyperspectral data. Section 3 discusses pre-processing techniques, existing correction techniques, and their limitations. Section 4 outlines different spectrum libraries, browse products, and summary parameters used for mineral identification on the Martian surface, along with their limitations. Geological characteristics used for mineral identification are described in Sec. 5, and challenges in using CRISM data for mineral identification are discussed in Sec. 6. Section 7 reviews different methodologies used for mineral classification, including the distance-based method, probabilistic method, unsupervised, and neural network approach. The authors highlight major findings of minerals on the Martian surface in Sec. 8. Sections 9 and 10 discuss validation techniques, the conclusion, and future exploration. The paper aims to provide a general understanding of mineral classification using CRISM.

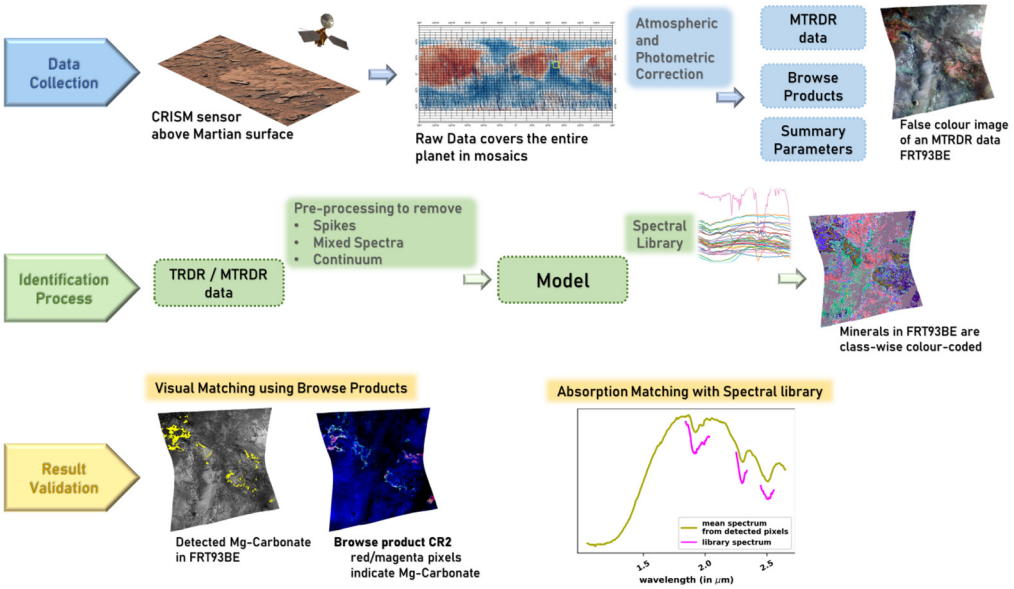

Fig. 3 A diagram highlighting the steps of the mineral mapping procedure on the Martian surface.

Table 1 Specifications of different MRO sensors.

Sensor	Spectral range (μm)	Spatial resolution	No. of bands	Objective
HiRISE[7]	0.4 to 0.7	0.6 m	1	• Capture high-resolution Martian surface images • Identify potential landing sites
CTX[8]	0.5 to 0.8	6 m	1	• Provide contextual imaging data • Support HiRISE and surface analysis
CRISM[9]	0.3 to 3.9	18 to 200 m	544	• Create global mineralogical and atmospheric maps • Study Martian surface and atmosphere composition
MCS[10]	0.3 to 4.5	5 km	9	• Study Martian atmosphere using IR • Understand climate and atmospheric evolution
MARCI[8]	0.2 to 0.8	Visible: 1 to 7 km; UV: 10 to 30 km	Visible-5	• Analyze Martian regional morphology • Understand Martian geological features
SHARAD[11]	12 to 20	15 m	—	• Detect subsurface features using radar • Investigate subsurface structures on Mars

2 Data Description for CRISM Data

The MRO was launched on August 12, 2005, following the loss of two previous Martian missions, the Mars Climate Orbiter (1998) and Mars Polar Lander (1999). MRO is equipped with several scientific instruments, including the High-Resolution Imaging Science Experiment (HiRISE), Mars Color Imager (MARCI), Context Imagery (CTX), Mars Climate Sounder (MCS), and Shallow Radar (SHARAD). Different specifications of these sensors are presented in Table 1.

These instruments are specifically designed to study different aspects of Mars, such as its geology, atmosphere, surface, climate, and the possibility of habitability.

The CRISM was the seventh successful operation to Mars orbiting at an altitude of 300 km in a sun-synchronous near-polar orbit. The CRISM instrument detects visible near-infrared (VNIR) wavelength by the "S" detector in the range 364 to 1055 nm, while infrared (IR) wavelength is detected by the "L" detector in the range 1.1 to 3.9 μm with a sampling of 6.55 nm per channel. The mission consisted of two phases: the multispectral mode and the targeted mode. In the multispectral mode, global mineral characterization was carried out with 72 selected channels operating at a resolution of 100 to 200 m per pixel, while the gimbal was positioned at the nadir. The data were collected at a frequency of 15 to 20 Hz. This mode was crucial in confirming the presence of hydrous movement on the Mars surface, which was difficult to detect with prior Mars-orbiting spectrometers due to their low spatial and spectral resolution. The targeted mode, covered a wide swath width of 9.5 to 12 km. This heightened spatial and spectral resolution offered an enhanced capability for in-depth analysis and comprehensive characterization of the Martian surface, surpassing what was achievable with the multispectral mode. The detailed description of CRISM data for different observing modes is shown in Table 2.[9,12]

3 Atmospheric Correction for CRISM Data

In this section, the significance of pre-processing CRISM hyperspectral data from Mars to enhance the quality and efficiency of mineral mapping is explored. The section also sheds light on the third objective of the MRO mission, which focuses on studying seasonal changes in atmospheric dust and ice aerosols and gathering additional details about the Martian atmosphere. Here, the use of two techniques—volcanic scan correction and the DISORT model—is emphasized to eliminate dominant atmospheric gas contributions in the near-IR spectra. By employing these techniques, the MRO mission is able to attain accurate characterization of seasonal

Table 2 Characteristics of different CRISM observing modes and their data products.[9,12]

Observing modes	Observation and mapping type	Resolution	Coverage and description
Targeted (hyperspectral) (positioned at gimbaled)	Full resolution targeted (FRT)	• Spatial resolution: 18 m/pixel @ 300 km • Spectral resolution: 544	• 6500 per Mars year • FRT is high-priority targeted data whereas HRL and HRS have limited data volume
	Half resolution short-targeted (HRS) and half resolution long-targeted (HRL)	• Spatial resolution: 36 m/pixel @ 300 km • Spectral resolution: 544	
Atmospheric (positioned both at gimbaled and nadir)	Emission phase function	• Spatial resolution: 200 m/pixel @ 300 km • Spectral resolution: 544	• Two orbits in every 2 months
	Tracking optical depth	• Spatial resolution: 200×900 m/pixel @ 300 km • Spectral resolution: 544	• Free-standing for atmospheric monitoring
Multispectral (positioned at nadir)	Multi-spectral survey	• Spatial resolution: 200 m/pixel @ 300 km • Spectral resolution: >72	• 80% of Martian surface • MSP has long strips for Global mapping
	Multi-spectral windows	• Spatial resolution: 100 m/pixel @ 300 km • Spectral resolution: 72	

fluctuations in suspended dust particles and icy aerosols. In addition, these methods provide supplementary data concerning the Martian atmosphere, contributing to a more comprehensive understanding of its properties.

3.1 Volcano Scan

Volcano scan is an empirical correction method that is designed to remove CO_2 absorption in the near-IR range of spectrum 1 to 2.6 μm. This method is based on previously derived transmission spectra and is applied empirically to remove the absorption of atmospheric gas. Low- and high-altitude spectra taken over Olympus Mons are used to obtain the necessary spectra, and the Beer–Lambert Law is utilized to calculate the transmission spectra.[13] The images are generally processed for reflectance using the CRISM Analysis Tools (CAT).[14]

The initial step is to transform the spectral radiance observed by the sensor, which is measured in units of watts per square meter per steradian per micrometer, to I/F, which is the ratio of the radiance detected by the sensor to the solar irradiance, divided by π. This converted data are then stored in the Experimental Data Record (EDR). Following this, the Photometric Lambertian correction is carried out to modify the bidirectional reflectance characteristics of the Lambertian surface and convert the data to a standard illumination geometry resulting in Lambert albedo. The ratio shift correction is then performed to evaluate the systematic cross-track residual structure, which is a ground plane along-track striping, and creates a correction frame based on inter-column ratio statistics supported cross-track structure. Then, the empirical geometric normalization is conducted to characterize and correct the geometric dependencies that arise from the continually changing geometry of CRISM-targeted observations wavelength-dependent along-track gradients. Finally, the empirical smile correction is performed to characterize and correct a radiometric residual related to a spectral smile, an instrument optical artifact, and wavelength-dependent asymmetric cross-track gradients. Figure 4 shows the process.

Once all the corrections are applied, the resulting value is stored in a targeted reduced data record (TRDR), which contains important information, such as latitude, longitude, incidence angle, emission angle, and phase angle. This information is used for map projection and post-processing corrections. A summary product is then calculated, and a browse product is created. Finally, after the map projection and pre-processing steps, spectral indices are derived and the map-projected targeted reduced data record (MTRDR) is obtained. How these summary products are used for mineral identification is provided in a later section.

3.2 Discrete Ordinates Radiative Transfer

DISORT is a powerful radiative transfer model widely utilized to replicate the propagation of light through a scattering medium like a planetary surface or atmosphere.[15] It finds extensive usage in remote sensing applications to simulate the interaction of light with planetary atmospheres and surfaces. In the context of CRISM data, DISORT can be employed to mimic the radiative transfer of sunlight through the Martian atmosphere and its reflection and scattering by the surface features. By comparing the simulated outcomes with the actual CRISM data, vital information regarding the composition and structure of the Martian surface can be deduced.

The DISORT model is a complex process that requires multiple inputs and steps to correct atmospheric effects. These steps include photometric, atmospheric, and thermal corrections, as well as the retrieval of various parameters from lookup tables. Figure 5 shows the different lookup tables used in the model. The photometric step begins by calibrating the raw data in EDR format to TRDR, considering various viewing and incidence angles. Next, using the latitude, longitude, topography, and apparent solar time associated with a specific pixel retrieved from the appropriate DDR, the column abundances of atmospheric elements and aerosols are procured from a lookup table called ADR_CL. In addition, the model obtains information regarding surface slope azimuth and magnitude, thermal inertia, dust, and ice aerosol capacities, as well as surface temperature for each pixel location. Subsequently, the values for each I/F (reflectance) at every wavelength in the scene are obtained from corresponding pixel locations in the DDR and ADR. To account for any necessary corrections, a pre-computed multiplicative correction retrieved from the lookup table ADR_AC is applied. The ultimate output of the DISORT model is the calculation of surface I/F, representing the theoretical Lambert albedo under ideal conditions with normal illumination and viewing geometry, disregarding atmospheric effects and thermal emission.

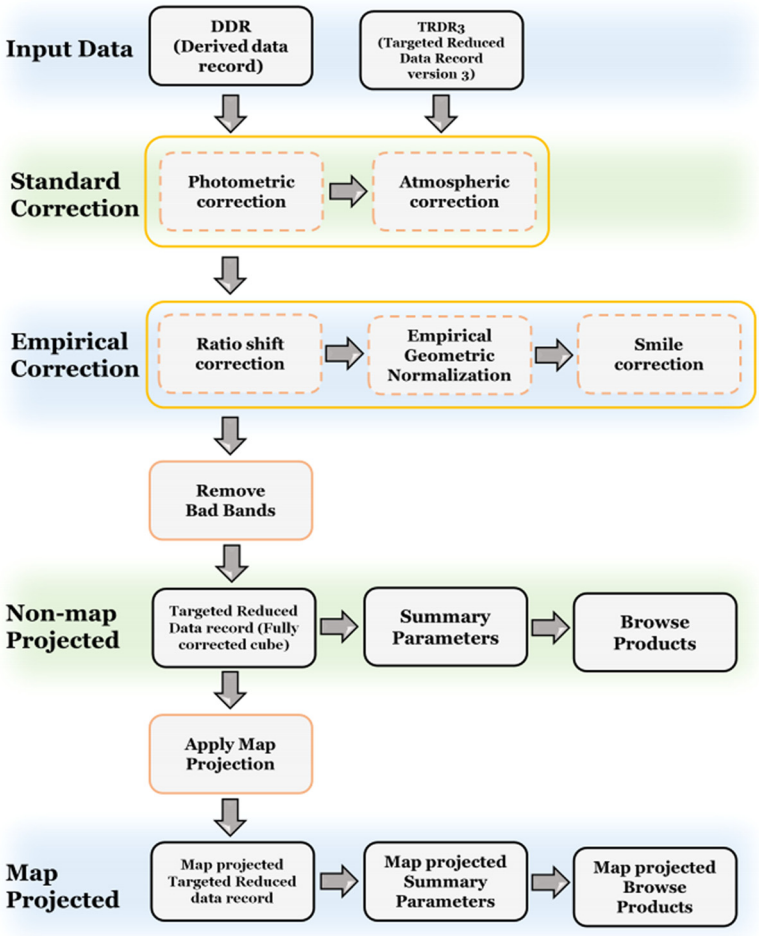

Fig. 4 Volcano scan correction method: sequential processing of TRDR3 data along with DDR to yield MTRDR data.

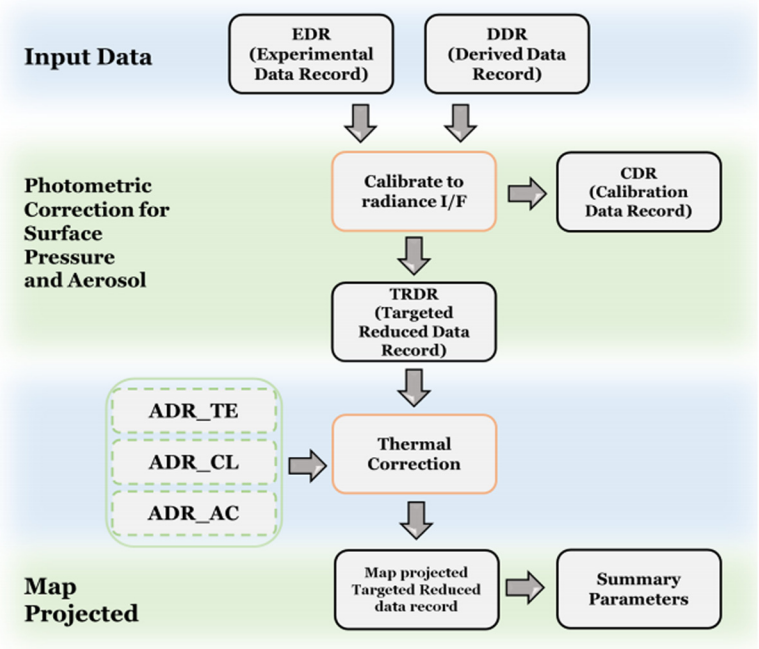

Fig. 5 DISORT model: sequential processing of EDR data along with DDR to yield MTRDR data.

Limitations: Both volcano scan and DISORT are commonly used methods for correcting and analyzing CRISM data; however, they do have certain limitations.

1. The volcano scan correction method is specifically designed for volcanic regions and may not be applicable to non-volcanic regions. Similarly, DISORT may not be suitable for all types of surface materials or atmospheric conditions.
2. Both methods require significant computational resources and time to process large amounts of data. This can limit their use for large-scale analysis or real-time applications.
3. Both methods rely on certain assumptions about the surface and atmospheric properties of Mars and may have uncertainties in their results. For example, the volcano scan correction method assumes a specific scattering phase function for the surface, which may not be accurate in all cases.
4. Both methods require accurate calibration and validation of the CRISM data, which can be challenging and may introduce errors in the analysis. Overall, while volcano scan correction and DISORT are useful tools for analyzing CRISM data, they should be used with caution and in conjunction with other methods to ensure accurate and reliable results.

4 Summary Parameters and Browse Products

This section presents a concise overview of the products that result from the atmospheric correction process, namely the summary parameters and browse products. These products play a crucial role in the interpretation of spectral data from Mars. Summary parameters represent a single parameter value that captures the spectral properties of specific mineralogy. These values are derived using different formulas applied to combinations of spectral bands, designed by the field experts.[5] Another important product of the atmospheric correction process is the CRISM browse product, which is a combination of thematically related summary parameters to form different false-color images. This product shows spectral variation associated with different mineral groups, such as ice, phyllosilicates, mafics, sulfates, carbonates, and hydrated silica groups of minerals in distinguishable colors. This product is useful for identifying minerals on the Martian surface visually. The optimal implementation of these parameters is critical for accurate interpretation of the data.

4.1 Summary Parameter

Initially, 44 summary parameters were given in Ref. 6 by Pelkey et al. based on multispectral images which were later updated in Ref. 16 by Viviano et al. with 60 summary parameters based on the hyperspectral images. Viviano et al. used these summary parameters to study the mineralogy and geology of several regions on Mars, including the Nili Fossae area and the Medusae Fossae Formation. These are derived from the following measures which are calculated from reflectances in key wavelengths.

- Band-depth ratio measures the relative depth of two absorption features in the spectrum of a given region. The two features used in Ref. 16 are associated with iron- and magnesium-rich phyllosilicates, which are indicators of aqueous alteration on Mars.
- Spectral slope measures the rate of change of reflectance or radiance with a wavelength in the visible and near-IR parts of the spectrum. Spectral slope can be used to infer the composition and grain size of surface materials.
- Integrated band area measures the area under an absorption feature in the spectrum of a given region. The absorption feature used in Ref. 16 is associated with olivine, a mineral that is common in basaltic rocks on Mars.
- Band center position measures the location of the center of an absorption feature in the spectrum of a given pre-computed absorption feature used in Ref. 16 and is associated with pyroxene, a mineral that is also common in basaltic rocks on Mars.

These summary parameters provide valuable information about the elements and physical properties of the Martian region and also are widely used for mineral identification. Table 3 presents some of these summary parameters along with their standard formulas.

Table 3 Different Summary parameters for CRISM hyperspectral data.

Parameter name	Examples	Standard formula
Reflectance (R)	R440 (0.44 μm reflectance),	Based on absorption at particular reflectance
	R530 (0.53 μm reflectance),	
	R600 (0.60 μm reflectance)	
Band ratio (BR)	RBR (for reflectances at 0.7 and 0.4 μm)	$\frac{R_{c_1}}{Rc_2}$
	IRR1 (for reflectances at 0.8 and 1.2 μm)	where
	IRR2 (for reflectances at 2.5 and 2.2 μm)	R_{c_1} is the reflectance for band 1
	IRR3 (for reflectances at 3.7 and 3.5 μm)	R_{c_2} is the reflectance for band 2
Spectral slope	SLOPE1 (spectral slope 1)	$\frac{R_{c_1}-R_{c_2}}{\lambda_{c_1}-\lambda_{c_2}}$
Spectral variance	VAR (1.0 to 2.3 μm) variance in spectra	variance in the fitted curve between 1 and 2.3 μm
Band depth (BD)	BD2165 (2.16 μm) band depth due to Al-OH,	$\mathrm{BD}(\lambda_c) = 1 - \frac{R_c}{R_c^*} = \left(1 - \frac{R_c}{aR_s + bR_L}\right)$
	BD2190 (2.19 μm) band depth due to Al-OH	where
		R_c = Reflectance at the center wavelength λ_c
		$R_c^* = (a * R_s + b * R_l)$ is derived from the continuum fit across the band
	BD2100 (2.10 μm) band-depth due to shift in shifted H_2O	$b = \frac{(\lambda_c - \lambda_s)}{(\lambda_l - \lambda_s)}$, $a = 1 - b$

Table 3 (*Continued*).

Parameter name	Examples	Standard formula
Inverse band depth (BH)	SH600 (0.6 μm)	$\mathrm{BH}(\lambda_c) = 1 - \frac{R_c^*}{R_c} = \left(1 - \frac{aR_s + bR_L}{R_c}\right)$
	SH770 (0.77 μm), where SH is the shoulder point	Note: two defining absorption features of ferric oxides overlap in the characteristic spectrum
Doublet parameter	DOUB2200 (0.16 and 2.21 μm band depth - doublet),	$\mathrm{GEOM}(\lambda_{c_1}, \lambda_{c_2}) = \sqrt{(\mathrm{BD}(\lambda_{c_1}) * \mathrm{BD}(\lambda_{c_2}))}$
	MIN2345_2537 and MIN2295_2480 (due to Fe/Mg carbonate overtone and band-depth in metal-OH)	$\mathrm{MIN}(\lambda_{c_1}, \lambda_{c_2}) = \mathrm{MIN}[\mathrm{BD}(\lambda_{c_1}), \mathrm{BD}(\lambda_{c_2})]$ where GEOM and MIN is geometric mean and minimum of two band depth
Broad band	OLINDEX2, HCPINDEX2	Combining multiple band depth $\mathrm{INDEX}(\lambda_{c_1}, \lambda_{c_2}, \ldots, \lambda_{c_n}) = D_1(\mathrm{BD}(\lambda_{c_1})) + D_2(\mathrm{BD}(\lambda_{c_2})) + \ldots + D_n(\mathrm{BD}(\lambda_{c_n}))$

Limitation in mineral identification: The use of summary parameters for identifying minerals on the Martian surface using has several limitations, such as,

- Spectral variability: The spectral response of minerals can vary significantly depending on factors, such as grain size, composition, and hydration state. Therefore, summary parameters that rely on a single spectral measurement may not be able to distinguish between different mineral species.
- Surface mixtures: The Martian surface can contain mixtures of different minerals, making it difficult to identify individual species. In some cases, summary parameters may not be able to differentiate between mixtures of similar minerals.
- Instrument noise: CRISM data can contain noise and artifacts that can affect the accuracy of summary parameters. This can lead to false positives or negatives in mineral identification.
- Spatial resolution: The spatial resolution of CRISM data is limited, which can make it difficult to identify minerals in small or complex geological features.
- Lack of ground truth: The identification of minerals using summary parameters is often based on spectral libraries and models, which may not accurately represent the Martian surface. In addition, there is limited ground truth data available for mineral identification on Mars, which can make it challenging to validate the results.

In summary, the use of summary parameters for identifying minerals on the Martian surface using CRISM data has several limitations, and these should be taken into account when interpreting the results.

4.2 Browse Product

A browse product is created by combining three summary product composites, resulting in a false-color image that allows for visual identification of minerals and analysis of their distribution map. This technique proves particularly useful in distinguishing subtle variations in phyllosilicate species, surpassing the capabilities of the original PHY product. The PFM and PAL browse products, in particular, exhibit enhanced sensitivity to such variations. The PFM product utilizes RGB composites of BD2355, D2300, and BD2290 to provide insights into Fe/Mg-phyllosilicates. In this composite, the existence of prehnite or chlorite is represented by red and yellow colors, while cyan colors generally show the existence of Fe/Mg smectites. On the other hand, the PHY product, with RGB composites of D2300, D2200, and BD1900r2, portrays all Fe/Mg-phyllosilicates as inseparable red or magenta given that possess similar hydration bands. The PAL product, with RGB composites of BD2210_2, BD2190, and BD2165, offers insights specifically related to Al-OH materials. In this composite, Al smectites are depicted as cyan, while kaolinites appear light or white in color. Similarly, the PHY product represents all Al-OH segments as indistinguishable green or cyan if they possess comparable hydration bands. In addition, the HYS product, utilizing RGB composites of MIN2250, BD2250, and BD1900r2, further identifies Si/Al-hydroxylated minerals. In this composite, hydrated silica is depicted as light red or yellow, while Al-OH minerals are represented as cyan. To accommodate variations in summary product values across scenes, each summary product is individually stretched and converted into an 8-bit RGB channel composition for the browse product. Figure 6 lists some of the commonly used browse products, their RGB composites, and associated color meanings.

5 Spectral Library

In remote sensing, a spectrum consists of measurements of how much light is absorbed or reflected at different wavelengths by a particular material. A spectral library is a collection of spectra built as a reference database by experts for different types of materials, such as vegetation, soil, water, minerals, and man-made features such as roads and buildings. For the minerals on the Martian surface, many spectral libraries have been created by compiling spectrum data from common materials for almost 50 years and made available easily by research organizations for the Martian surface which most widely used such as CRISM spectral library,[5] MICA type spectral library,[16] and Reflectance Experiment Laboratory (RELAB) library.[17] These spectral libraries are important resources for planetary scientists studying Mars. These enable remote

BP Name RGB Channels	Significance	BP Image	BP Name RGB Channels	Significance	BP Image
True colour **(TRU)** R600 R530 R440	Enhanced CRISM I/F image after atmospheric and photometric correction	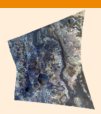	VNIR albedo **(VNA)** R770 R770 R770	Photometric corrected CRISM I/F at 770nm Used for correlation between spectra and mineralogy.	
Ferrous mineral **(FEM)** BD530 2 SH600 2 BDI1000VIS	**Red**: ferric oxides **Green:** textural effects **Blue:** mafic minerals	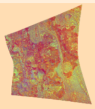	Ferrous mineral second version **(FM2)** BD530 2 BD920 2 BDI1000VIS	**Red**: ferric oxides **Green:** coarser-grained Fe minerals **Blue:** mafic minerals	
Tandem **(TAN)** R2529 IRA R770	alse colour CRISM I/F image.		IR albedo **(IRA)** R1300 R1300 R1300	Photometrically corrected CRISM I/F image at wavelength 1330nm.	
False colour **(FAL)** R2529 R1506 R1080.	**Red:** Olivine-Rich mineral **Green:** mostly shows clay. **Gray/Brown:** Basaltic minerals		Mafic mineral **(MAF)** OLIINDEX3 LCPINDEX2 HCPINDEX2.	**Red:** olivine and Fe phyllosilicates. **Green/Cyan:** HCP **Blue/Magenta:** LCP	
Hydrated minerals **(HYD)** SINDEX2 BD2100_2 BD1900_2.	**Red/Magenta:** polyhydrated sulfate **Green/yellow:** monohydrated sulfate **Blue:** clay,carbonate and zeolite	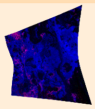	Phyllosilicates **(PHY)** D2300 D2200 BD1900r2.	**Red/Magenta**: hydrated phyllosilcates **Green/cyan**: hydrated silica **Blue:** Sulfates, carbonate and hydrated silica	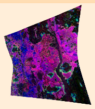
Phyllosilicates with Fe/Mg and carbonate **(PFM)** BD2355 D2300 BD2290	**Red/yellow**: prehnite, chlorite, and Ca/Fe **cyan:** Fe/Mg smectites, Mg carbonate.	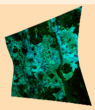	Phyllosilicates with Al **(PAL)** BD2210_2 BD2190 BD2165	**Red/yellow**: smectites or hydrated silica **green/cyan:** alunite **light-white:** kaolinite	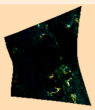
Hydrated silica **(HYS)** MIN2250 BD2250 BD1900r2	**Red/yellow:** hydrated silica **yellow:** jarosite **cyan:** Al-OH minerals **Blue:** hydrated minerals	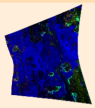	Ices (ICE) BD1900_2 BD1500_2 BD1435	**Red:** sulfates, clays **Green:** water-ice **Blue:** ice	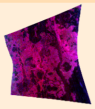
ices version 2 **(ICE_2)** R3920 BD1500_2 BD1435	**Red:** ice free surfaces **Green:** strong absorption at 1.5 micrometer **Blue:** sharp absorption at 1.435 for ice frost	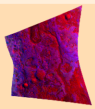	Chloride **(CHL)** ISLOPE BD3000 IRR2	**Red:** chloride deposits **Green:** hydrated mineral **Blue:** ice frost	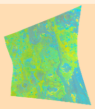
Carbonate **(CAR)** D2300 BD2500H2 BD1900_2	**Red/Magenta:** Fe/Mg-phyllosilicates **yellowish-white:** Mg carbonates **Blue:** hydrated minerals	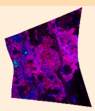	Carbonate version 2 **(CR2)** MIN2295_2480 MIN2345_2537 CINDEX2	**Red/Magenta:** Mg carbonates **Green/cyan:** Fe/Ca carbonates	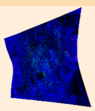

Fig. 6 Different browse products of a CRISM hyperspectral data FRTC518 from Gale Crater region.

sensing analysts to identify the observed materials in the image by comparing the spectral signature of the materials to known spectral signatures in the library and map their distribution and abundance. In addition, these libraries guide mission planning by identifying areas of interest, aid in understanding the Martian environment by studying the distribution of water and ice, and help develop new analytical techniques for planetary surface study. By analyzing the spectral data in these libraries, scientists can gain new insights and make new discoveries about Mars.

5.1 CRISM Spectral Library

NASA has built a Planetary data science system (PDS) by incorporating spectra from the CRISM spectrum library as well as from other sensors. The CRISM spectral library is a significant resource for studying the mineralogy and composition of Mars, and it has numerous important applications in planetary science. This library released on March 10, 2006, is the first ground truth library to allow the interpretation and analysis of minerals on the Planetary surface. There are currently 2260 spectrum analyses altogether collected from Mars, Moon, and Earth surface, consisting of 1134 natural and artificial Mars samples in the CRISM spectral library, which is organized in a hierarchical framework. All of the spectra in this library are samples with the same spectral resolution of CRISM data and were interpolated using linear interpolation to remove the atmospheric obstruction and CO_2 absorption under appropriate environmental conditions of the Martian surface. The material origin (Mars, Moon, and Earth surface), classification

(rocks, minerals, etc.), mineral class (phyllosilicates, sulfates, etc.), diverse mineral species (prehnite), and device for measuring CRISM data are all included in the content of this spectrum library. This library is incorporated within the CAT tool and accessible on the PDS geoscience node. PDS provides a web-based interface where data can be searched, displayed, and downloaded by adding location information (latitude, longitude) of the surface.

5.2 MICA-Type Spectral Library

The MICA-type spectral library, derived from a CRISM sensor comprising multispectral and hyperspectral images, serves as a widely accepted and utilized standard for mineral identification and validation on the Martian surface. This comprehensive library is composed of data collected over a span of more than 7 years from CRISM TRDR data, along with recently discovered data from diverse Martian locations captured by the CRISM instrument. The library is the result of continuous efforts by researchers to expand the collection of spectral data available for the interpretation of Martian surface mineralogy. The library contains three types of spectra: numerator, denominator, and ratioed I/F spectra. These spectra are used for mineral identification and mapping and have proven to be valuable tools in the study of the geology and mineralogy of Mars. The MICA library has a total of 31 minerals grouped into six different types: mafic and iron oxide, sulfates, phyllosilicates, carbonates, hydrated silicates, and ice.[16] The planetary data and the CRISM website both provide access to the information corresponding to the MICA-type spectral library.[16]

5.3 RELAB Library

The Reflectance Experiment Laboratory spectral library is a collection of visible to near-IR reflectance spectra of minerals, rocks, and other planetary materials. The library was developed by the Planetary Spectroscopy Laboratory at Brown University and is widely used in planetary science and remote sensing applications. The RELAB library contains over 2000 spectra of minerals and rocks that are relevant to planetary science, including samples from the Moon, Mars, asteroids, and other planetary bodies. The spectra were acquired using a variety of laboratory instruments and under different environmental conditions, such as different illumination angles, temperatures, and pressures. One of the unique features of the RELAB library is its high spectral resolution, which allows for the identification of subtle spectral features that may not be visible in lower-resolution spectra. The library also includes detailed metadata for each sample, such as mineralogy, physical properties, and sample preparation methods. The RELAB library is widely used in remote sensing applications for planetary exploration, including the analysis of data from several space missions, such as the MRO, Lunar Reconnaissance Orbiter, and the Dawn spacecraft. The library is publicly available and can be accessed online through the Planetary Data System (PDS) website, which allows for easy access and sharing of data.[17]

6 Surface Mineralogy of Martian Surface

The Martian surface is a treasure trove of minerals that hold valuable information about the planet's geological history and potential for habitability. Various mineral groups can be found on Mars, each with its own significance.[16] The mafic and iron oxide group, including minerals such as olivine, pyroxene, and magnetite, are indicators of past volcanic and impact processes. The sulfate group, such as gypsum and jarosite, and the phyllosilicates group, including clay minerals, suggest the presence of liquid water in the past and are potential markers for past or present microbial life. Carbonates, such as calcite and magnesite, provide insights into Mars' past climate and water cycle. Hydrated silicates, such as serpentine and chlorite, form through hydrothermal alteration. Ice minerals, including water ice and carbon dioxide ice, are found in the polar ice caps and the atmosphere, respectively. Studying these minerals through remote sensing techniques enables scientists to unravel Mars' evolution and its potential for supporting life.[6,16] Future missions will continue to focus on exploring these diverse mineral types for astrobiological investigations. By understanding the surface characteristics of minerals, including their spectral signatures and spatial distribution, researchers can enhance mineral mapping, mineral exploration, and the development of materials science applications. The significant

Mineral Groups	Mineral Name	Absorption Features
Mafic and Iron Oxides	Hematite	absorption at 0.53 μm and close to 0.9 μm
	Fe/Mg Olivine	Broad absorption near 1 μm
	Plagioclase	Broad absorption at 1.25 and 1.31 μm
	Low calcium Pyroxene	absorption at 0.9 and 1.8 μm
	High calcium Pyroxene	absorption at 1.05 and 2.3 μm
Sulfates	Monohydrated Sulphate	absorption at 2.1 μm
	Polyhydrated Sulphate	absorption 2.1,1.4,1.9 and 2.4 μm
	Alunite	doublet near 1.4 and 2.2 μm absorption near 1.76 and 2.3 μm
	Hydroxy Fe-Sulphate	strong absorption at 1.48, 1.75, and 2.23 μm
	Jarosite	absorption at 0.9, 1.47,1.85 and 2.25 μm
	Gypsum	triplet band absorption near 1.4 to 1.5 μm
	Bassanite	strong band absorption near 1.93–1.94 μm multiple features near 2.1–2.3 μm
Phyllosilicates	Kaolinite	prominent absorption at 1.4 μm a doublet near 2.2 μm
	Al-Smectite	absorptions 2.26 and 2.35 μm doublet near 2.2 μm
	Illite / Muscovite	absorption at 1.9 and 2.3 μm
	Fe-Smectite	absorptions at 1.4, 1.9 and 2.28-2.32 μm
	Mg-Smectite	narrow band absorption at 1.4 μm absorption drop at 2.35 μm
	Talc	strong absorption near 1.9 μm
	Serpentine	OH overtone at 1.39 μm weaker band at 2.1 μm absorption centered at 2.32 and 2.5 μm
	Chlorite	strong absorption near 2.3-2.35 μm
	Prehnite	absorption between 2.35 and 2.36 μm
Hydrated Silicates and Halaides	Hydrated Silica	absorption at 2.33 and 2.53 μm
	Epidote	absorption at 2.30 and 2.51 μm
	Analcime	triplet band absorption near 1.4 to 1.5 μm
	Chloride	strong band near 1.93–1.94 μm multiple features near 2.1–2.3 μm
Ices	H2O-Ice	Broad absorption at 1.5 μm
	CO2-Ice	tiny absorption at 1.435 μm
Carbonate	Fe/Ca carbonate	absorption at 2.33 and 2.53 μm
	Mg carbonate	strong absorption band at 2.30 and 2.51 μm

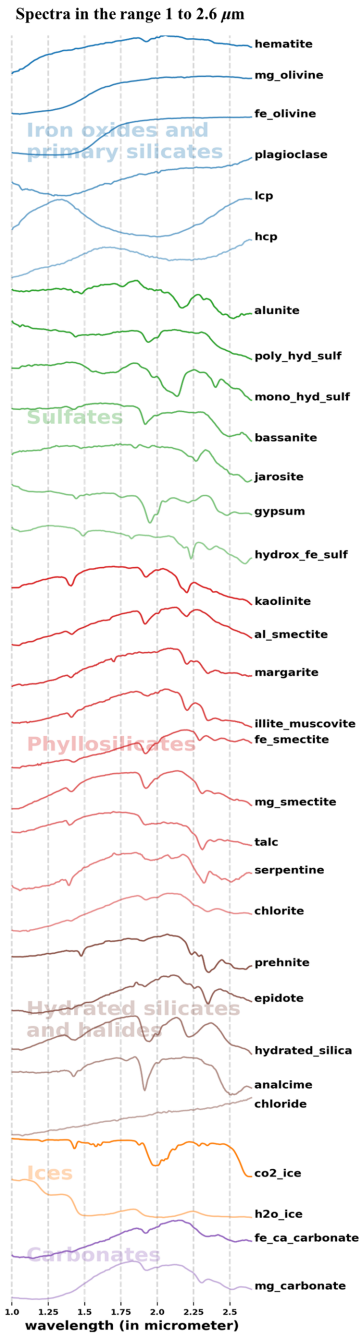

Fig. 7 Spectral features of some minerals found on the Martian surface and the spectra from MICA library.

absorption features of some of the most common minerals found on the Martian surface are discussed below. These minerals are also summarized in Fig. 7 for reference.

6.1 Mafic Minerals and Iron Oxides

This mineral category primarily consists of iron and magnesium-rich minerals, including hematite, olivine, plagioclase, and pyroxene. Hematite detection, which is attributed to the Fe^{3+} transition within the 0.4 to 0.9 μm wavelength range, was accomplished using the CRISM detector. The absorption features at ~0.53 and 0.9 μm are crucial for identifying and distinguishing Fe^{3+}-bearing minerals, such as hematite, jarosite, and nanophase oxides.[18] Olivine, a mineral-rich in magnesium and iron, exhibits broad absorption around 1 μm, which is further intensified

by the electronic transition of iron within its structure, defining its spectral characteristics. In contrast, pyroxene spectra show broad absorption peaks centered around 1 and 2 μm, resulting from the domain transition of iron in multifaceted coordination. The pyroxene mineral group includes low calcium pyroxene (LCP) and high calcium pyroxene (HCP). In LCP minerals, the absorption band is centered at ~0.9 and 1.8 μm whereas in HCP, the bands are located within 1.05 and 2.3 μm. The precise positions of these mineral absorptions are influenced by the calcium content within the pyroxene structure.[19,20] Plagioclase, another significant mineral found on the Martian surface, exhibits broad absorption characteristics centered at 1.25 and 1.31 μm, primarily on account of minor substitution of Fe^{2+} for Ca^{2+}. Plagioclase is typically detectable when other mafic minerals are present in an abundance of <5%.[21]

6.2 Sulfates

The sulfates group of minerals is abundantly present and widely distributed across the Martian surface. Notable concentrations of sulfates have been identified in Meridiani Planum and adjacent areas of Arabi, as well as within the internal layered deposits on the canyon system's floor and associated chaotic zones in Valles Marineris. The dunes surrounding the northern polar icecap are primarily composed of sulfate gypsum.[22,23] Unlike mono-hydrated sulfates, which exhibit variations in water vibrational combinations depending on the cation, spectra of poly-hydrated sulfates display an absorption feature at 2.1 μm, resulting from a combination of elongation and flexion oscillations of water molecules. The detection of poly-hydrated sulfates is challenging due to the presence of another hydrous mineral that exhibits absorptions within 1.4, 1.9, and 2.4 μm.[24] Several sulfate species with distinctive spectral characteristics have been identified. Jarosite, for instance, displays absorption peaks centered at 1.47 and 1.85 μm.[25] Bassanite exhibits a prominent band within 1.93 to 1.94 μm, along with multiple absorption characteristics in the range of 2.1 to 2.3 μm attributed to H_2O.[26] Gypsum spectra reveal a distinct band in the range of 1.4 to 1.5 μm, while alunite exhibits a doublet near 1.4 and 2.2 μm, accompanied by additional absorptions near 1.76 and 2.3 μm.[27]

6.3 Phyllosilicates

Phyllosilicates comprise a diverse range of minerals found on the Martian surface, each exhibiting unique spectral characteristics. For instance, kaolinite prominently shows an absorption peak at 1.4 μm and a doublet near 2.2 μm, resulting from the vibrational modes of the hydroxyl group and the Al-OH band. AI-smectite and mica also display a doublet near 2.2 μm but can be distinguished by the extra channel at 2.26 and 2.35 μm.[28] Fe/Mg-phyllosilicates are prevalent in various geological settings, including stratified deposits, exposed crust outcrops, and occasionally in alluvial fans or deltas.[29] This group encompasses Fe-smectite, Mg-smectite, serpentine, talc, prehnite, chlorite, and margarite.[30] The identification of Fe/Mg-phyllosilicates is based on their compositional H_2O and OH absorption features at near 1.4 μm and a decrease at 2.35 μm feature, which shifts to elongated wavelengths as Mg replaces Fe.[28] Mg-smectite exhibits narrower absorption characteristics around 1.4 μm and a decrease at 2.35 μm, talc demonstrates a strong absorption near 1.9 μm near 2.3 to 2.35 μm attributed to the Mg-OH band,[31] and prehnite exhibits absorption between 2.35 and 2.36 μm. Serpentine is identified by a diagnostic weaker band at 2.1 μm, an OH overtone at 1.39 μm, and absorptions centered at 2.32 and 2.5 μm. However, conclusive observations of serpentine pose challenges due to the requirement of a high signal strength relative to noise to identify the superficial yet diagnostically significant 2.1 μm feature.

6.4 Hydrated Silicates and Halides

The mineral group consisting of epidote, zeolite, and chloride displays specific absorption characteristics at 2.21 to 2.22 μm arising from Si-OH amalgamation vibration, particularly at 2.26, 1.91, and 1.4 μm because of compositional H_2O and OH. Epidote exhibits a strong absorption near 2.24 and 2.35 μm, with a weaker absorption at 1.55 μm, enabling its differentiation from spectrally similar mixtures, such as chlorite, illite, and calcite.[30,32] Zeolite exhibits notable absorptions within 1.4, 1.9, and 2.4 μm, which share spectral similarities with poly-hydrated sulfates. However, zeolite can be distinguished from poly-hydrated sulfates by its intense and subtle absorption at 2.5 and 1.79 μm.[33] On the other hand, chlorides do not display distinct

serpentine attributes in the visible and near-IR spectrum; however, they demonstrate unusually amplified thermal IR radiative properties. This is accompanied by a decreasing slope in the spectral profile as the wave numbers decrease. Chlorides demonstrate a distinctive combination of a blue slope in the visible and near-IR range, a red slope in the IR range, and a relatively less prominent 3 μm H_2O feature. This suggests their hydrous nature compared to other surface materials detected by CRISM.

6.5 Ices

The unique spectral characteristics of ice, such as the broad absorption around 1.5 μm associated with crystalline H_2O ice and the small absorption feature at 1.435 μm in CO_2 ice spectra, offer a means to distinguish between different ice types. The narrow absorption at 1.435 μm is particularly advantageous because it is unaffected by atmospheric CO_2 bands at 2 μm, and it is ~2.3 times more potent than the subsequent secondary CO_2 ice bands at 2.281 μm.[34]

6.6 Carbonates

Carbonates are formed when water captures atmospheric carbon dioxide, leading to the formation of a mineral group known as carbonates, which includes Mg-carbonate and Fe/Ca carbonate. The presence of carbonates can be identified by their characteristic absorption peaks at 2.3 and 2.5 μm, corresponding to vibrations of the C-O bond. Fe/Ca carbonate exhibits specific absorption peaks at 2.33 and 2.53 μm, while Mg-dominant carbonates shift to 2.30 and 2.51 μm. The abundance of calcium carbonates can be attributed to the weathering of Ca-dominant silicate rocks and the previous existence of carbonate rocks. The current saltwater on Mars is oversaturated with calcium carbonate. On the other hand, deposits of magnesium carbonate provide insights into past aqueous activity on the Martian surface.[35,36]

7 Geological Information of Different Study Areas

Mars is known for its fascinating geology, which can be divided into two hemispheres, the northern and southern hemispheres shown in Fig. 8. The northern hemisphere is characterized by a large and flat plain known as the Vastitas Borealis, which is home to several large craters, including the Lyot Crater and the Korolev Crater.[38,39] In contrast, the southern hemisphere of Mars is much more rugged and varied, with several deep canyons, including the Valles Marineris, which is the largest canyon system in the solar system, and several large volcanoes, including the massive Olympus Mons, which is the largest volcano in the solar system.[40,41] Fossae are another important geological feature on the Martian surface, with the Cerberus

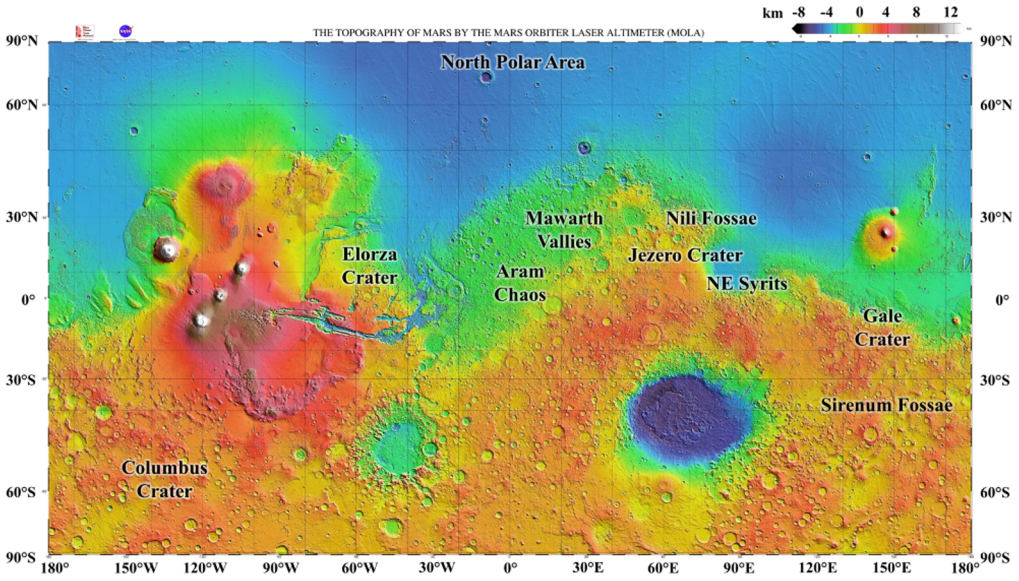

Fig. 8 Mola elevation map showing location on the Martian surface where the mineral has previously been studied.[37]

Fossae and the Valles Marineris being the largest systems. The Syrtis Major is a dark, circular region on the planet's surface that is thought to be a large volcanic plain. The Hellas Planitia and the Argyre Planitia are the two largest impact basins in the southern hemisphere of Mars, and both are characterized by large, flat plains. Craters are the most prominent feature on Mars, with the Hellas Planitia being the largest crater on the planet. Mars is also home to several large and significant valleys, including the Valles Marineris, Mawarth Vallies, Ma'adim Vallis, and the Valles Alpes, which were mostly created by past, severe flooding. The MRO CRISM instrument has detected clays in the Jezero Crater, indicating the past presence of water. This makes Jezero Crater a prime location for the Mars 2020 mission's objective of exploring a potentially habitable environment for remnants of past life. Mawrth Vallis was also considered a potential landing site for the Mars Science Laboratory (MSL) mission in 2011, but Gale was ultimately chosen as the landing site for the Curiosity mission due to indications of water by the presence of clays and sulfate minerals. Researchers have already explored various areas on the Martian surface some of which are listed in Table 4.

8 Challenges Exist in Mineral Identification in CRISM Data

The complexity of hyperspectral data presents significant challenges in data processing and analysis. One of these challenges is identifying and removing bad bands from the data caused by various factors, such as atmospheric interference, sensor noise, detector malfunctions, or data transmission errors. Domain and scale inconsistency is also a significant issue in the CRISM hyperspectral dataset due to variations in atmospheric conditions, mineral composition, and other factors. For example, however, different minerals in the MICA library have spectra that depend on various wavelengths, ranging from 430 bands for gypsum to 480 bands for bassanite. To eliminate domain inconsistency, various interpolation techniques are commonly used, while standardization or normalization is utilized to adjust the data to a uniform scale so that it can be compared and analyzed more easily. Despite applying atmospheric and photometric corrections, residual fluctuation noises in the form of spikes or small kinks can persist in spectra, potentially obscuring significant features and introducing errors in scientific analysis. In the literature, researchers have employed several smoothing techniques to address this issue, including window-median filtering and Savitzky–Golay filtering, with the aim of mitigating such disturbances.[6,67,68] In this section, the two specific challenges associated with the spectra in CRISM hyperspectral images, the issue of mixed spectra and the presence of the continuum resulting from this, are examined in detail, aiming to provide a comprehensive understanding of their implications.

8.1 Mixed Spectra

The planetary surfaces are composed of a mixture of different minerals, rocks, and soils. In a scene, each object has its own unique spectral signature characterized by absorption or emission lines, representing reflectance values across different wavelengths. When hyperspectral imaging captures the light from all objects, their individual spectral signatures combine to form the overall spectral shape of the scene, resulting in spectral mixing as depicted in Fig. 9. For example, a pixel may contain a mixture of iron oxide minerals and silicates, which is different from the individual spectra of the pure endmembers. As the resulting spectrum reflects the combined spectral information of the objects rather than their individual features, it is very hard to detect the individual endmembers. To overcome these challenges, spectral unmixing techniques have been developed, allowing for the extraction of individual spectra and fractional abundances of different materials within each pixel. Some of these are highlighted below.

- Linear spectral unmixing (LSU)[69] assumes that each pixel's spectrum is a linear combination of pure endmember spectra and employs a linear equation to relate the observed spectrum to the endmember spectra and uses a least-squares approach for abundance estimation.
- Nonlinear spectral unmixing (NSU)[70] methods assume a nonlinear relationship between the pixel's spectrum and the endmember spectra. They can be more accurate than LSU when dealing with highly nonlinear relationships. NSU techniques include artificial neural networks (ANN), support vector machines, and decision trees.

Table 4 Different locations on the Martian surface with the dominant minerals.

Area	Major findings	References
Aram chaos	Monohydrated sulfate, nanophase ferric oxide	23
2.6°N, 21.5°W		
Columbus Crater	Kaolinite, polyhydrated sulfate, monohydrated sulphate	42
29.8°S, 166.1°W	Fe/Mg phyllosilicates, jarosite, alunite, kaolinite	43
	Gypsum, poly- and mono-hydrated Mg/Fe-sulfates, kaolonite	44
Mawrth Vallis	Fe smectite, alunite, Al smectite	45
	Fe/Mg-phyllosilicates, Al-phyllosilicates, hydrated silica	46
22.3°N, 343.5°E	Fe/Mg-smectite, Al-phyllosilicate, hydrated silica	47
Melas Chasma	Nontronite, jarosite, Al-clays, and leached clay	48
10.4°S, 72.7°W	Polyhydrated, monohydrated sulfates, and jarosite	49
	HCP and phyllosilicate	50
NE Syrtis	Low-calcium pyroxene, Fe/Mg smectite, olivine	51
	HCP, LCP	52
18°N, 77°E	Fe/Mg-smectite, LCP	53
Nili Fossae	Fe/Mg smectite, magnesium carbonate, olivine	54
	Kaolinite, nontronite, chlorite, and vermiculite	55
22°N, 75°E	Chlorite, prehnite, serpentine, kaolinite, potassium mica	56
	Prehnite, chlorite, silica	57
Kashira Crater	Kaolinite-group mineral halloysite	58
27.0°S, 341.7°E		
Elorza Crater	Phyllosilicates (vermiculite) and mafic silicates	59
304.8°E, 8.76°N		
North polar area	Gypsum	60
88°00′N, 15°00′E		
Sirenum Fossae	Kaolinite	44
35.57°S, 197.26°W		
South Syrtis	Ca/Fe carbonate, illite	61
18.855°N, 77.519°E		
Gale Crater	Olivine and high-calcium pyroxene	62
5°24′S, 137.8°E	Kaolinite, chlorites, smectite, jarosite	63
Jezero Crater	Mg-rich carbonate, olivine	64
18.38°N, 77.58°E	Fe/Mg-smectites, Al-phyllosilicates, carbonates	65
Robert Sharp Craters	Akaganeite	66
4.17°S, 133.42°E		

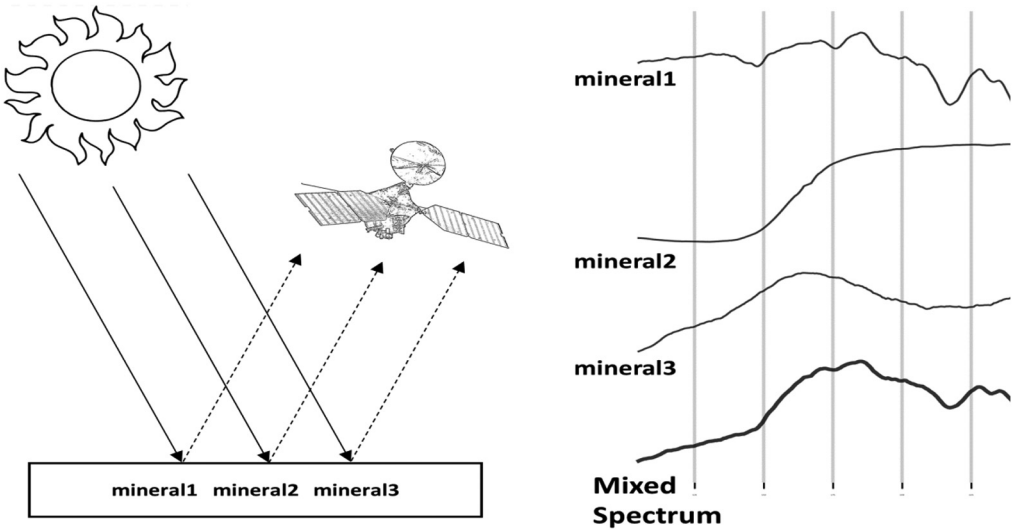

Fig. 9 The diagram depicts a surface (a pixel in hyperspectral data) containing three different minerals having distinct spectra. The spectrum captured from the surfaced is a mixed spectrum containing individual absorptions of those minerals.

- Independent component analysis (ICA)[71] is a statistical method that assumes the observed spectrum is a linear combination of statistically independent components. It has been used to map phyllosilicates on the Martian surface.
- Multiple endmember spectral mixture analysis (MESMA)[72] extends LSU by allowing multiple endmembers in each pixel. This technique is useful for cases with significant spectral variability within a pixel.
- Vertex component analysis (VCA)[73] is a geometric-based method that identifies pure endmembers by finding the vertices of a convex hull formed by the data points. It also assumes the mixed spectra as a linear combination of the endmember spectra.
- Band-pixel selection and smoothing (BPSS)[74] uses a smoothing algorithm to reduce the effect of noise in the data and then selects a subset of the spectral bands that are most informative for mineral identification.
- Multivariate curve resolution non-negative matrix factorization (MVC-NMF)[75] decomposes the mixed spectra into a set of endmembers and their corresponding abundance fractions using a non-negative matrix factorization (NMF) approach.
- **Multiple-endmember linear spectral unmixing model**[76] analyzes the mineralogical composition of the Martian surface using the OMEGA imaging spectrometer. It selects the best linear combination of spectra from a reference library to determine mineral composition. The analysis is restricted to the 1.0 to 2.5 μm wavelength range, and synthetic spectra are included in the library to account for variations in grain size and atmospheric scattering.

The LSU process is a rapid and convenient way to conduct an appropriate mathematical inversion and is time-saving enough to be carried out on large amounts of data. However, the coefficients obtained for each mineral are not simply related to their true abundance, so the method can only be used as a qualitative detection of components. Reference 77 investigated the capability of spectral unmixing techniques for analyzing hyperspectral images from Mars, specifically focusing on a selected CRISM image of the Russell mega dune. Seven state-of-the-art linear unmixing approaches are compared, and the quality of the results is estimated through correlation coefficients and average errors between the reconstructed and reference abundance maps. The authors of this work concluded that abundance maps provided by VCA, BPSS, and MVC-NMF are generally accurate and sufficient for initial planetary interpretation.

8.2 Presence of Continuum

A mixed spectrum possesses a smooth baseline shape, known as a continuum, that masks the individual spectral features. The continuum can also arise from various factors, such as

instrument artifacts and topographic illumination effects. Continuum alters the global curvature of the target spectrum as shown in Fig. 10. It is of utmost importance to eliminate the continuum from the analyzed spectrum and accurately discern its distinctive absorption characteristics in order to facilitate precise material identification. Imposed continuum removal (ICR) and apparent continuum removal (ACR) are two methods used for removing the continuum from a spectrum in order to enhance the unique absorption signatures. ICR involves fitting a polynomial or power-law model to the entire spectrum, assuming a known or confidently assumed continuum shape.[78] On the other hand, ACR selects local regions in the spectrum that lack spectral features and connects them to estimate the continuum for the full spectrum domain.[79] The estimated continuum is then subtracted or divided from the spectrum to nullify its effects.[80] ICR is preferred when the continuum shape is well-established, while ACR offers more flexibility and robustness in dealing with variations in the continuum shape:

$$\mathcal{C}(R) = R/C \quad \text{or} \quad \mathcal{C}(R) = R - C$$

where R is the spectrum being analyzed, C is the estimated continuum, and $\mathcal{C}(R)$ is the continuum-removed spectrum.

In the context of continuum removal in hyperspectral data, various methods exist, each with its own advantages and limitations. The convex hull method is commonly employed for short-wave infrared spectra due to their typically convex or flat nature. This method involves fitting an upper convex hull (UCH) to the spectrum to estimate the continuum.[81] However, there are several limitations to this approach. First, it assumes that the spectral signal has a convex shape, which may not hold true for all real-world spectra; second, this method is sensitive to outliers in the data; and lastly, this may not effectively remove the continuum from spectra with low-intensity signals. These can result in inaccurate peak identification and quantification, although, many researchers vouch for using simple continuum removal techniques, such as UCH.

Two variants of hull technique are present in the literature which involve calculating a segmented upper hull[82] and a linear local hull.[83] In Ref. 84, the authors extended the UCH method to propose a segmented curve-fitting method for continuum removal that detects more shoulder points within the segments generated by UCH to determine the distinct absorption signatures in a test spectrum more accurately. Another method, called reference spectral background removal (RSBR) eliminates the influence of unwanted contribution factors by simulating the background curve and removing it from the original spectrum.[85] Experimental comparisons showed that RSBR can more accurately extract absorption centers and widths from mixed spectra, regardless of variations in abundance, if endmembers are known priori. Another technique that uses a geometric hull[86] also has been successful in accurately determining the band-minima of the endmembers.

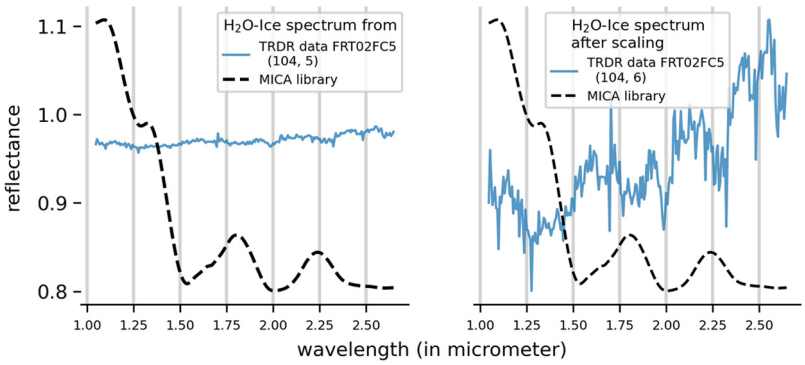

Fig. 10 The difference in global curvatures between the two H_2O–ice spectra in the left image is evident after the scaling operation in the right image.

9 Mineral Classification Models

Mineral identification on the Martian surface is fundamental to understanding the geological and geochemical processes that have shaped the planet's surface. The manual approach for mineral identification in CRISM images involves selecting a region of interest, which acts as the numerator, and an unremarkable region, which act as the denominator, to obtain the ratioed I/F CRISM image. The spectral rationing enhances the spectral absorption characteristics and reduces the multiplicative noise. These spectra are then visually compared with a spectral library to identify minerals based on their absorption features. However, this approach is time-consuming and requires tremendous manual labor. The identification of an unremarkable zone within the image possibly on the same line sample and finding the right match of numerator, denominator, and stretch limit requires immense domain expertise. As a result, there is a growing need for automated solutions. Initially, distance-based similarity-matching techniques were employed but struggled to capture semantic differences, rendering them inadequate for mineral identification. Therefore, alternative approaches, such as probabilistic, unsupervised, and neural network models, have been developed to address these limitations and demonstrate improved effectiveness in mineral identification. Some of the distance-based methods, as well as the alternative techniques, are discussed in this section, Table 5.

9.1 Distance-Based Matching Methods

Distance-based methods are used for mineral mapping because they are relatively simple to implement and can be used to quickly classify large amounts of hyperspectral data. The distance-based methods are based on the fact that minerals have unique chemical compositions and crystal structures that affect the way they reflect and absorb light. By computing the distance or angle between a pixel's spectrum signature and the spectra of reference minerals in a library, the pixel can be assigned to the mineral that bears the closest resemblance.

Table 5 Different genres of methods used in the literature for mineral identification in CRISM data.

Method genre	Method name	Study area	References
Distance-based matching	SAM	Jezero Crater	87
		Gale Crater	63
	ED	Jezero Crater	88
		Nili Fossae	89
	MD	Jezero Crater	90
		Mawrth Vallis	91
	MF	Nili Fossae	92
		Gale Crater	93
Distribution-based unsupervised methods	GMM	Nili Fossae	94
	HDP	Aram Chaos	95
	PO-HDP	Nili Fossae	96
	HBM	Gale Crater	97
Distance-based unsupervised methods	OPTICS, DEMUD	Nili Fossae	88
	SMACC, N-FINDR	Nili Fossae, Jezero Crater	98
Neural networks	DNN	Nili Fossae	99
	GAN	Jezero Crater	89
	Active learning-based classifier	Jezero Crater	89
	CNN, ANN, SVM, RFC	Jezero Crater, Mawrth Vallis	68

Euclidean distance (ED)[100] is a simple and commonly used distance metric that measures the straight-line distance between two points in spectral space. Mahalanobis distance (MD)[101] is a more complex metric that accounts for the correlations between the spectral bands and is, therefore, more robust than ED. Spectral angle mapper (SAM)[102] is based on the idea that the spectra of different minerals have different shapes in spectral space and that these shapes can be characterized by the angles between them. The main advantage of using SAM is that it is invariant with scale and illumination. Matched filtering (MF)[103] is based on the idea that the spectral signature of a pixel can be decomposed into a linear combination of the spectral signatures of the end members in the library and that the end member with the highest coefficient is the one that best represents the pixel.

Although the distance-based approach is so simple to map the mineral, very little literature exists on it. The main reason behind this similarity method is designed to capture the global difference between two vectors. On the contrary, mineral identification is based on similarity involving the presence of absorption dip with the wavelength ranges.

9.2 Distribution-Based Unsupervised Methods

Probabilistic methods are favored in mineral mapping due to their ability to provide an accurate and comprehensive characterization of mineralogy, surpassing traditional approaches based on thresholds or linear models. These methods offer several advantages. First, they allow for uncertainty quantification, enabling the estimation of mineral abundances and classifications with associated uncertainty. This is crucial when dealing with mineral mixtures or noisy spectral signatures. Second, probabilistic methods account for non-linearity, acknowledging that the relationship between reflectance spectra and mineral abundances is often non-linear. Linear models may not capture this accurately, making probabilistic methods more suitable for precise abundance estimation. Lastly, probabilistic methods exhibit robustness to outliers and noise in the data. Several widely employed probabilistic methods in this context are highlighted below.

- Gaussian mixture model (GMM)[104] is a parametric probability density function used to model the distribution of observed data by combining multiple Gaussian distributions. It aims to identify distinct mineral components in spectral data by representing their spectral signatures as Gaussian distributions. The GMM assumes that each pixel in the image contains a mixture of mineral components and estimates the proportion of each component in every pixel. To overcome limitations in handling skewed distributions or unknown numbers of components, the infinite Gaussian mixture model has been introduced. It allows for the estimation of inference and other component parameters in a unified process. However, to handle situations requiring non-Gaussian or differently shaped distributions, the infinite mixture of infinite Gaussian mixture model has been developed.[96] It is doubly non-parametric and enables the identification of the number of components for each cluster with various shapes and sizes.

  GMM is relatively simple and computationally efficient for mineral mapping, but it assumes Gaussian distributions for mineral spectral signatures and does not incorporate prior knowledge about mineral distributions in the region of interest, limiting its accuracy in some cases.
- Hierarchical Dirichlet process (HDP)[105] is a Bayesian non-parametric model that enables the clustering of data points into multiple groups based on their similarity, without requiring a predefined number of clusters. It provides a flexible framework for discovering latent structures in data. In the context of mineral identification using spectral data, the partially observed HDP (PO-HDP) is a variant of this model. The PO-HDP is specifically designed to identify the presence of various minerals within a specific region based on spectral information. It operates under the assumption that each pixel in a spectral image represents a mixture of different mineral components. By utilizing the spectral data, the model estimates the proportion of each mineral component within each pixel, allowing for accurate mineral identification and mapping. The PO-HDP offers a powerful approach for analyzing complex spectral datasets and extracting valuable information about the mineral composition of an area. Its Bayesian nature provides a robust and flexible framework for handling uncertainties and missing data.

- Hierarchical Bayesian model (HBM)[106] uses the observed data as a function of unknown parameters, which are themselves modeled as random variables. In the context of mineral mapping, the observed data could be spectral data collected from a satellite or airborne sensor, and the unknown parameters could be the proportions of different minerals present in each pixel of the image. One advantage of the HBM is that it is a flexible modeling framework that can be adapted to different data types and sources of prior knowledge. This prior information can be derived from geological maps, previous mineral surveys, or other sources of information. By incorporating prior knowledge into the model, the HBM can improve the accuracy and robustness of the mineral mapping results, allowing for the identification of mineral deposits correlated with certain geological features.

In Ref. 95, the authors used a bi-level Bayesian Gaussian mixture model that had shown promise in eliminating nonlinear noise and determining both high- and low-abundance mineral aspects in CRISM images, where GMM is implemented for the identification of the spectral and spatial distribution of minerals at pixel scale for each mineral class. This developed model made efficient, accurate, and scalable assessments toward automation of mineral identification by replacing traditional spectral analysis techniques.

9.3 Distance-Based Unsupervised Methods

The unsupervised classification approach is widely used for mineral characterization on the Martian surface due to the deficit of classified training data, as it does not require any prior knowledge of the end members. Unsupervised clustering methods find natural groupings on similar spectral characteristics in the unlabeled data and then match each group with the spectral library to assign a label. These methods also can identify new mineral types that may not be present in a pre-defined mineral library and help researchers discover new mineral types or identify previously unknown minerals.

- Ordering points to identify the clustering structure (OPTICS)[107] identifies the natural clustering structure of a dataset without assuming a fixed group of clusters or any previous information of the data distribution. It does this by defining a hierarchy of density-based clusters based on the concept of reachability distance. OPTICS algorithm is used in Ref. 88 to cluster super-pixels to reduce redundancy in identified minerals and make more confident from the respective region on the Martian surface, followed by DEMUD analysis on the super-pixels to assign a label based on threshold operation for anomaly detection to find rare minerals. This method has been applied to Hesperia Planum (Fe/Mg smectite), Aram Chaos (jarosite, kieserite), and Juventae Chasma (Mg-olivine, monohydrated sulfate).[88,108]
- SMACC[109] method constructs convex cones around each data point and then merges the cones that have similar spectral properties. N-FINDR[110] is another unsupervised algorithm that uses NMF to identify pure spectral endmembers in an iterative process. In Ref. 98, the authors used these methods on CRISM images and detected several dominant minerals, such as kalonite, carbonate, olivine, and phyllosilicates. Nevertheless, these methods can be time-consuming, and it is still necessary to identify the minerals of the suspected detections by comparing them with spectra obtained from laboratory analysis.

9.4 Neural Networks

Neural networks are renowned for their ability to uncover hidden patterns in data. However, they typically require a substantial amount of labeled training data, which can be a challenge when it comes to mineral identification on the Martian surface. The scarcity of ground truth or training data hinders the development of supervised learning models for this purpose. Currently, there are only a few studies that have employed neural network-based approaches with CRISM hyperspectral data for mineral exploration.[99] A recent investigation[95] tackled this concern by offering a dataset of labeled pixels sourced from 77 distinct TRDR images taken at numerous sites on Mars. The labeling process involved employing an HBM that estimates spectral pattern variations. These labeled pixels can prove to be a valuable asset for tasks, such as nonlinear noise reduction, operating as the training set for mineral identification models, and validated using TRDR or MTRDR data. Another approach[68] involved creating training data by augmenting the

spectra available in the MICA spectral library keeping the key absorption signatures in the mineral spectra unaltered while providing sufficient diversity. This allowed for the development of neural network models for mineral identification using CRISM data.

In Ref. 68, the authors have provided a novel augmentation method and preprocessing pipeline that incorporated a feature extraction method to capture the distinctive absorption patterns in spectra, along with a few traditional early data processing phases. They implemented both a shallow ANN model[111] and a shallow convolutional neural network (CNN) model[112] to compare the effectiveness of the proposed feature extraction step. The study yielded satisfactory results, indicating that further improvements in performance could be achieved by refining the preprocessing steps, exploring advanced feature extraction techniques and incorporating more sophisticated learning models.

In Ref. 113, the authors proposed an active learning-based classifier for neutral spectra, aiming to reduce the number of labeled examples required for training. They employed a selective sampling technique that evaluates the quality of each neutral spectrum individually, minimizing the need for expert labeling and reducing costs. The algorithm utilizes the query-by-committee approach, iteratively selecting the most informative data points for labeling and training a committee of models on the same training set. Through multiple iterations, the model improves over time, with a particular emphasis on addressing problematic areas. The subjective nature of labeling allows the proposed framework to learn complex boundaries in classification tasks.

In Ref. 89, the generative models were employed to improve the distinguishability of spectra. The authors manually labeled samples from 30 CRISM images, using MICA identification for classification. A detailed preprocessing pipeline was presented to prepare the data for the generative model. The study demonstrated that the features acquired by the generative adversarial network (GAN) exhibited greater efficacy in distinguishing mineral signatures within the CRISM database when compared to summary parameters and traditional similarity metrics. For pixel classification, the spectral angular mapper (SAM) metric was used to identify the best match between the target pixel and the spectra generated by the models.

10 Validation Techniques

Result validation is crucial for accurate mineral identification in CRISM data on Mars, helping scientists confirm specific minerals and prevent misidentification. By enhancing scientific understanding, these techniques provide insights into Martian geology, its history, and potential habitability. The lack of ground truth data on Mars poses challenges for traditional field-based validation, but statistical analysis and comparison with previous studies offer effective means to overcome this limitation. For example, the presence of a specific mineral can be expected in a particular region based on its geological history. Result validation using browse products and a spectral library also provides a better understanding of the efficacy of a model. Combining multiple techniques allows scientists to validate identified minerals in CRISM data, improving the accuracy and completeness of Martian surface mineral maps.

The CRISM image FRT93BE (latitude: 19.1N, longitude: 283.5W), which is given in Fig. 11, obtained from the Jezero Crater region, has been used in Ref. 68 for mineral identification purposes. Using the proposed ANN model, the dominant minerals detected in the scene include Mg-carbonate, HCP, and Mg-Smectite, which align with findings from a previous study in Ref. 89. The PHY (RGB composites—R: D2300; G: D2200; B: BD1900R2) and PFM (RGB composites: R: BD2355; G: D2300; B: BD2290) browse products provide valuable insights into the component of hydroxylated and phyllosilicate group minerals. In the PHY product, the presence of indistinguishable Fe/Mg-Smectites is represented by red/magenta colors, while in the PFM product, they exhibit a cyan tinge, considering the equivalent strength of hydration bands. The MAF (RGB composites: R: OLINDEX3; G: LCPINDEX2; B: HCPINDEX2) browse product focuses on mafic mineral investigation, where Fe-phyllosilicate and olivine simultaneously display a characteristic bowl-shaped absorption in the 1.0 to 1.7 μm range. This absorption is visualized in the MAF product as a red color. Specifically, HCPINDEX2, which is responsive to broad absorption at 2 μm associated with pyroxene, effectively distinguishes HCP from other spectral signatures that exhibit convexity centered at 1.3 and 1.5 μm. Consequently, HCP shows

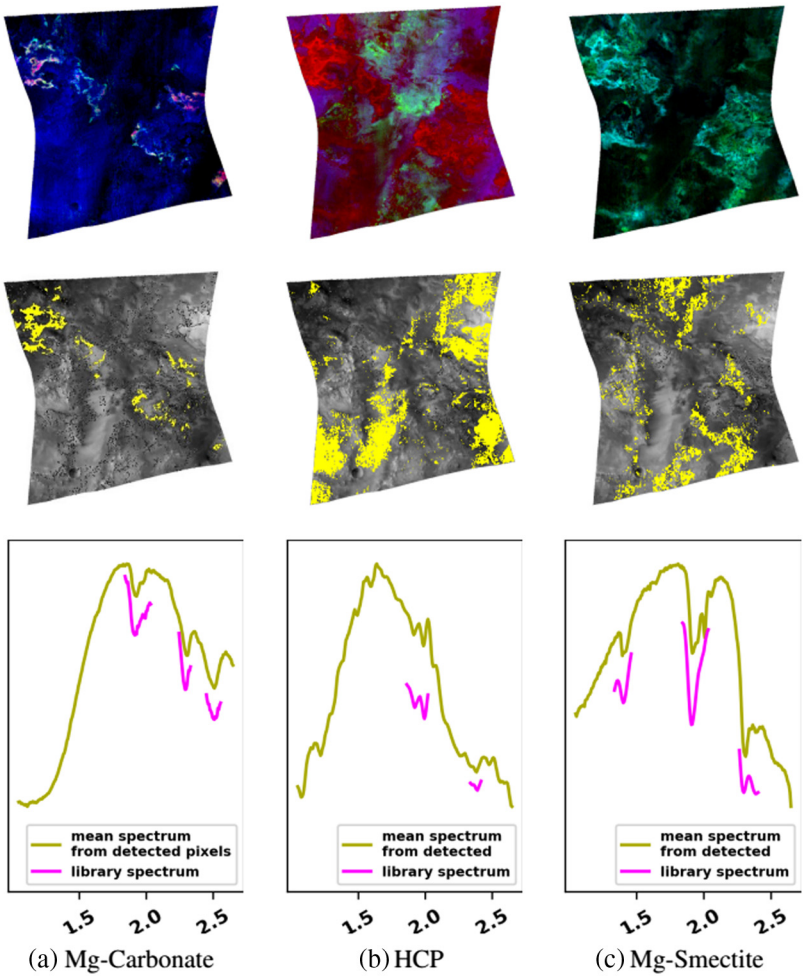

Fig. 11 Detected dominant minerals in CRISM MTRDR data FRT93BE. (Top row) Browse products (left: CR2, red/magenta colored pixels indicate Mg-carbonate), (middle: MAF, blue/magenta colored pixels indicate HCP), (right: PFM, cyan colored pixels indicate Fe/Mg-Smectite); (middle row) minerals detected by the ANN model given in Ref. 68; (bottom row) absorption feature matching between mean spectra of detected pixels and corresponding spectra from MICA library.[16] (a) Mg-carbonate, (b) HCP, and (c) Mg-smectite.

as a blue/magenta cover in the MAF product. Figure 11 shows these findings, including a comparison between the important absorption features observed in the mean spectra of the detected minerals and the associated spectra in the MICA spectral library.

11 Conclusion and Future Prospectives

CRISM covering a broad spectral range in the VNIR and IR has revolutionized mineral identification on the Martian surface, providing unprecedented detail in probing the composition of Martian minerals. The derived browse products and summary parameters, obtained through extensive photometric and atmospheric correction procedures, play a crucial role in interpreting and visualizing mineralogical data. Summary parameters effectively capture the distinctive absorption features of minerals, while browse products generate false-color images that enhance the visibility of mineral distribution. The integration of machine learning techniques has shown promising results in automating the process of mineral identification. The ongoing missions and technological advancements will further enhance our understanding of Martian mineralogy and its history.

Despite the significance of the aforementioned technique for mineral investigation on the Martian area using CRISM data, a universal and optimal procedure for precise classification and

quantification is yet to be established. Several challenges, including noise interference in CRISM MTRDR data, continue to pose formidable obstacles. Even after applying standard noise correction methods, residual noise persists, resulting in the presence of a continuum in spectra that can lead to misclassification. Although numerous continuum reduction techniques have been proposed in the literature, they have not completely eliminated noise from the data. Thus, the development of more effective continuum removal techniques is imperative to enhance the accuracy of mineral classification. Furthermore, the extraction of pure pixels from CRISM images remains a formidable task due to the prevalence of mixed spectra caused by instrument artifacts and noise. While summary parameter characteristics have been widely employed for mineral identification, manual selection of appropriate numerator and denominator combinations for different locations is time-consuming and susceptible to errors, particularly in the presence of instrument artifacts and noise, which can give rise to false mineral detections. Consequently, alternative approaches that do not solely rely on summary parameters have been explored extensively in previous studies to overcome these limitations.

Distance-based mineral categorization is rare in CRISM data due to scale and global shape differences. Unsupervised learning is the most suitable method for mineral classification, while the Bayesian model shows potential for integrating CRISM hyperspectral data. Limited implementation of supervised learning exists due to insufficient training data, but progress is being made through data augmentation approaches. GAN models also have shown potential for addressing the challenge. The utilization of neural network models in planetary exploration holds great potential for enhancing the community's capacity to rapidly and accurately map compositional units in remote-sensing data on a large scale. This advancement may open doors for the development of more sophisticated and efficient second-generation algorithms. Neural network approaches offer several advantages in the context of mineral mapping. They are capable of handling intricate spectral signatures that may pose challenges for visual interpretation, and they demonstrate the ability to efficiently and accurately classify vast amounts of data. Moreover, supervised learning techniques enable the identification of minerals that are not easily discernible through visual inspection, while also facilitating the mapping of mineral distribution and abundance within a given study area.

Machine learning methods in hyperspectral remote sensing become more computationally demanding as the data size increases. It is important to choose the right approach based on the specific application and experimental conditions, as there is no one-size-fits-all solution. Although there are several machine learning algorithms available, their practical implementation for mineral identification using CRISM hyperspectral data is still limited. Collaborative efforts between scientists, engineers, and data analysts will play a crucial role in overcoming the existing challenges and pushing the boundaries of CRISM research.

Code and Data Availability

The links of the available data and experimental results are included as references, cited at the intended places in the manuscript.

Acknowledgments

The authors would like to thank the associate editor Professor Wendy Zhou and the anonymous reviewers for the constructive comments which improved the quality of this article. The authors have no relevant financial interests in the manuscript and no other potential conflicts of interest to disclose.

References

1. J. F. Mustard et al., "Hydrated silicate minerals on Mars observed by the Mars Reconnaissance Orbiter CRISM instrument," *Nature* **454**(7202), 305–309 (2008).
2. L. Wendt et al., "Sulfates and iron oxides in Ophir Chasma, Mars, based on OMEGA and CRISM observations," *Icarus* **213**(1), 86–103 (2011).
3. J. Skok et al., "A spectroscopic analysis of Martian Crater central peaks: formation of the ancient crust," *J. Geophys. Res. Planets* **117**(E11) (2012).
4. B. L. Ehlmann et al., "Mineralogy of the Martian surface," *Annu. Rev. Earth Planet. Sci.* **42**(1), 291–315 (2014).

5. S. Murchie et al., "Compact Reconnaissance Imaging Spectrometer for Mars (CRISM) on Mars Reconnaissance Orbiter (MRO)," *J. Geophys. Res. Planets* **112**(E5) (2007).
6. S. Pelkey et al., "CRISM multispectral summary products: parameterizing mineral diversity on Mars from reflectance," *J. Geophys. Res. Planets* **112**(E8) (2007).
7. A. S. McEwen et al., "Mars Reconnaissance Orbiter's high resolution imaging science experiment (HiRISE)," *J. Geophys. Res. Planets* **112**(E5) (2007).
8. M. C. Malin et al., "Context camera investigation on board the Mars Reconnaissance Orbiter," *J. Geophys. Res. Planets* **112**(E5) (2007).
9. S. L. Murchie et al., "Compact Reconnaissance Imaging Spectrometer for Mars investigation and data set from the Mars Reconnaissance Orbiter's primary science phase," *J. Geophys. Res. Planets* **114**(E2) (2009).
10. D. McCleese et al., "Mars Climate Sounder: an investigation of thermal and water vapor structure, dust and condensate distributions in the atmosphere, and energy balance of the polar regions," *J. Geophys. Res. Planets* **112**(E5) (2007).
11. R. Seu et al., "SHARAD: the MRO 2005 shallow radar," *Planet. Space Sci.* **52**(1–3), 157–166 (2004).
12. F. P. Seelos et al., "The CRISM investigation in Mars orbit: overview, history, and delivered data products," *Icarus* 115612 (2023).
13. S. Wiseman et al., "Characterization of artifacts introduced by the empirical volcano-scan atmospheric correction commonly applied to CRISM and OMEGA near-infrared spectra," *Icarus* **269**, 111–121 (2016).
14. P. C. McGuire et al., "An improvement to the volcano-scan algorithm for atmospheric correction of CRISM and OMEGA spectral data," *Planet. Space Sci.* **57**(7), 809–815 (2009).
15. P. C. McGuire et al., "MRO/CRISM retrieval of surface Lambert albedos for multispectral mapping of Mars with disort-based radiative transfer modeling: phase 1—using historical climatology for temperatures, aerosol optical depths, and atmospheric pressures," *IEEE Trans. Geosci. Remote Sens.* **46**(12), 4020–4040 (2008).
16. C. E. Viviano et al., "Revised CRISM spectral parameters and summary products based on the currently detected mineral diversity on Mars," *J. Geophys. Res. Planets* **119**(6), 1403–1431 (2014).
17. C. M. Pieters1, "RELAB library citation," (2004). https://www.planetary.brown.edu/relab/.
18. R. V. Morris et al., "Mineralogy, composition, and alteration of Mars Pathfinder rocks and soils: evidence from multispectral, elemental, and magnetic data on terrestrial analogue, SNC meteorite, and Pathfinder samples," *J. Geophys. Res. Planets* **105**(E1), 1757–1817 (2000).
19. R. G. Burns, "Rates and mechanisms of chemical weathering of ferromagnesian silicate minerals on Mars," *Geochim. et Cosmochim. Acta* **57**(19), 4555–4574 (1993).
20. J. B. Adams, "Visible and near-infrared diffuse reflectance spectra of pyroxenes as applied to remote sensing of solid objects in the solar system," *J. Geophys. Res.* **79**(32), 4829–4836 (1974).
21. J. J. Wray et al., "Prolonged magmatic activity on Mars inferred from the detection of felsic rocks," *Nat. Geosci.* **6**(12), 1013–1017 (2013).
22. A. Gendrin et al., "Sulfates in Martian layered terrains: the OMEGA/Mars Express view," *Science* **307**(5715), 1587–1591 (2005).
23. K. A. Lichtenberg et al., "Stratigraphy of hydrated sulfates in the sedimentary deposits of Aram Chaos, Mars," *J. Geophys. Res. Planets* **115**(E6) (2010).
24. M. Craig et al., "Alteration of hydration absorption features in reflectance spectra of selected sulfates in a low pressure environment: 0.45 – 4.3 μm," in *37th Annu. Lunar and Planet. Sci. Conf.*, p. 2112 (2006).
25. W. H. Farrand et al., "Discovery of jarosite within the Mawrth Vallis region of Mars: implications for the geologic history of the region," *Icarus* **204**(2), 478–488 (2009).
26. J. J. Wray et al., "Identification of the Ca-sulfate bassanite in Mawrth Vallis, Mars," *Icarus* **209**(2), 416–421 (2010).
27. G. Swayze et al., "Discovery of the acid-sulfate mineral alunite in Terra Sirenum, Mars, using MRO CRISM: possible evidence for acid-saline lacustrine deposits?" in *AGU Fall Meet. Abstracts*, Vol. 2008, p. P44A–04 (2008).
28. B. L. Ehlmann et al., "Evidence for low-grade metamorphism, hydrothermal alteration, and diagenesis on Mars from phyllosilicate mineral assemblages," *Clays Clay Minerals* **59**(4), 359–377 (2011).
29. B. L. Ehlmann et al., "Subsurface water and clay mineral formation during the early history of Mars," *Nature* **479**(7371), 53–60 (2011).
30. J. Carter et al., "Hydrous minerals on Mars as seen by the CRISM and OMEGA imaging spectrometers: updated global view," *J. Geophys. Res. Planets* **118**(4), 831–858 (2013).
31. W. M. Calvin and T. V. King, "Spectral characteristics of iron-bearing phyllosilicates: comparison to Orgueil (CI1), Murchison and Murray (CM2)," *Meteoritics Planet. Sci.* **32**(5), 693–701 (1997).
32. J. B. Dalton et al., "Identification of spectrally similar materials using the USGS Tetracorder algorithm: the calcite–epidote–chlorite problem," *Remote Sens. Environ.* **89**(4), 455–466 (2004).
33. S. L. Murchie et al., "A synthesis of Martian aqueous mineralogy after 1 Mars year of observations from the Mars Reconnaissance Orbiter," *J. Geophys. Res. Planets* **114**(E2) (2009).

34. U. Fink and G. Sill, "The infrared spectral properties of frozen volatiles," in *IAU Colloq. 61: Comet Discov., Stat., and Observ. Selection*, pp. 164–202 (1982).
35. C. S. Edwards and B. L. Ehlmann, "Carbon sequestration on Mars," *Geology* **43**(10), 863–866 (2015).
36. J. C. Walker, P. Hays, and J. F. Kasting, "A negative feedback mechanism for the long-term stabilization of Earth's surface temperature," *J. Geophys. Res. Oceans* **86**(C10), 9776–9782 (1981).
37. D. E. Smith et al., "Mars Orbiter Laser Altimeter: experiment summary after the first year of global mapping of Mars," *J. Geophys. Res. Planets* **106**(E10), 23689–23722 (2001).
38. S. J. Conway et al., "Climate-driven deposition of water ice and the formation of mounds in craters in Mars' north polar region," *Icarus* **220**(1), 174–193 (2012).
39. P. Russell and J. Head III, "The Martian hydrosphere/cryosphere system: implications of the absence of hydrologic activity at Lyot Crater," *Geophys. Res. Lett.* **29**(17), 8-1–8-4 (2002).
40. D. E. Smith et al., "The gravity field of Mars: results from Mars Global Surveyor," *Science* **286**(5437), 94–97 (1999).
41. E. C. Morris and K. L. Tanaka, *Geologic maps of the Olympus Mons region of Mars*, The Survey (1994).
42. J. Wray et al., "Columbus Crater and other possible paleolakes in Terra Sirenum, Mars," in *40th Annu. Lunar and Planet. Sci. Conf.*, p. 1896 (2009).
43. L. Chaves et al., "Acidic environments in Columbus Crater, Mars: implications for habitability," in *49th Annu. Lunar and Planet. Sci. Conf.*, No. 2083, p. 1744 (2018).
44. J. Wray et al., "Columbus Crater and other possible groundwater-fed paleolakes of Terra Sirenum, Mars," *J. Geophys. Res. Planets* **116**(E1) (2011).
45. A. Sessa, J. Wray, and J. Bishop, "Discovery of alunite in candidate ExoMars landing site, Mawrth Vallis: evidence for localized evaporative environments," in *49th Annu. Lunar and Planet. Sci. Conf.*, No. 2083, p. 2983 (2018).
46. E. Noe Dobrea et al., "Mineralogy and stratigraphy of phyllosilicate-bearing and dark mantling units in the greater Mawrth Vallis/west Arabia Terra area: constraints on geological origin," *J. Geophys. Res. Planets* **115**(E7) (2010).
47. J. R. Michalski et al., "The Mawrth Vallis region of Mars: a potential landing site for the Mars Science Laboratory (MSL) mission," *Astrobiology* **10**(7), 687–703 (2010).
48. C. M. Weitz, E. N. Dobrea, and J. J. Wray, "Mixtures of clays and sulfates within deposits in western Melas Chasma, Mars," *Icarus* **251**, 291–314 (2015).
49. L. H. Roach et al., "Hydrated mineral stratigraphy of Ius Chasma, Valles Marineris," *Icarus* **206**(1), 253–268 (2010).
50. T. Sivasankari and S. Arivazhagan, "An overview of morphological and composition investigation of Melas Chasma of Valles Marineris," in *Ninth Int. Conf. Mars*, Vol. 2089, p. 6145 (2019).
51. B. L. Ehlmann and J. F. Mustard, "An *in-situ* record of major environmental transitions on early Mars at northeast Syrtis Major," *Geophys. Res. Lett.* **39**(11) (2012).
52. H. Clenet et al., "A systematic mapping procedure based on the Modified Gaussian Model to characterize magmatic units from olivine/pyroxenes mixtures: application to the Syrtis Major volcanic shield on Mars," *J. Geophys. Res. Planets* **118**(8), 1632–1655 (2013).
53. E. L. Scheller and B. L. Ehlmann, "Composition, stratigraphy, and geological history of the Noachian basement surrounding the Isidis impact basin," *J. Geophys. Res. Planets* **125**(7), e2019JE006190 (2020).
54. B. Ehlmann, J. Mustard, and S. Murchie, "Detection of serpentine on Mars by MRO-CRISM and possible relationship with olivine and magnesium carbonate in Nili Fossae," in *40th Annu. Lunar and Planet. Sci. Conf.*, p. 1787 (2009).
55. Y. Xue, Y. Yang, and L. Yu, "Mineral composition of the Martian Gale and Nili Fossae regions from Mars Reconnaissance Orbiter CRISM images," *Planet. Space Sci.* **163**, 97–105 (2018).
56. B. L. Ehlmann et al., "Identification of hydrated silicate minerals on Mars using MRO-CRISM: geologic context near Nili Fossae and implications for aqueous alteration," *J. Geophys. Res. Planets* **114**(E2) (2009).
57. C. E. Viviano, J. E. Moersch, and H. Y. McSween, "Implications for early hydrothermal environments on Mars through the spectral evidence for carbonation and chloritization reactions in the Nili Fossae region," *J. Geophys. Res. Planets* **118**(9), 1858–1872 (2013).
58. T. A. Goudge et al., "Integrating CRISM and TES hyperspectral data to characterize a halloysite-bearing deposit in Kashira Crater, Mars," *Icarus* **250**, 165–187 (2015).
59. N. Jain and P. Chauhan, "Elorza Crater on Mars: identification of phyllosilicate-bearing minerals by MRO-CRISM," *Proc. SPIE* **9880**, 322–335 (2016).
60. K. E. Fishbaugh et al., "On the origin of gypsum in the Mars north polar region," *J. Geophys. Res. Planets* **112**(E7) (2007).
61. T. D. Glotch and A. D. Rogers, "Evidence for magma-carbonate interaction beneath Syrtis Major, Mars," *J. Geophys. Res. Planets* **118**(1), 126–137 (2013).
62. K. D. Seelos et al., "Mineralogy of the MSL Curiosity landing site in Gale Crater as observed by MRO/CRISM," *Geophys. Res. Lett.* **41**(14), 4880–4887 (2014).

63. Y. Xue and S. Jin, "Martian minerals components at Gale Crater detected by MRO CRISM hyperspectral images," in *2nd Int. Symp. on Instrum. and Meas., Sens. Netw. and Autom. (IMSNA)*, IEEE, pp. 1067–1070 (2013).
64. T. A. Goudge et al., "Assessing the mineralogy of the watershed and fan deposits of the Jezero Crater paleolake system, Mars," *J. Geophys. Res. Planets* **120**(4), 775–808 (2015).
65. M. Salvatore et al., "Bulk mineralogy of the NE Syrtis and Jezero Crater regions of Mars derived through thermal infrared spectral analyses," *Icarus* **301**, 76–96 (2018).
66. T. Peretyazhko et al., "Effect of solution pH and chloride concentration on akaganeite precipitation: implications for akaganeite formation on Mars," *J. Geophys. Res. Planets* **123**(8), 2211–2222 (2018).
67. J. Carter et al., "Automated processing of planetary hyperspectral datasets for the extraction of weak mineral signatures and applications to CRISM observations of hydrated silicates on Mars," *Planet. Space Sci.* **76**, 53–67 (2013).
68. P. Kumari et al., "A fully-automated framework for mineral identification on Martian surface using supervised learning models," *IEEE Access* **11**, 13121–13137 (2023).
69. M. Graña and A. D'Anjou, "Feature extraction by linear spectral unmixing," *Lect. Notes Comput. Sci.* **3213**, 692–698 (2004).
70. S. Hamylton, "A comparison of spatially explicit and classic regression modelling of live coral cover using hyperspectral remote-sensing data in the Al Wajh lagoon, Red Sea," *Int. J. Geogr. Inf. Sci.* **26**(11), 2161–2175 (2012).
71. T.-W. Lee and T.-W. Lee, *Independent Component Analysis*, Springer (1998).
72. C. Quintano, A. Fernández-Manso, and D. A. Roberts, "Multiple Endmember Spectral Mixture Analysis (MESMA) to map burn severity levels from Landsat images in Mediterranean countries," *Remote Sens. Environ.* **136**, 76–88 (2013).
73. J. M. Nascimento and J. M. Dias, "Vertex component analysis: a fast algorithm to unmix hyperspectral data," *IEEE Trans. Geosci. Remote Sens.* **43**(4), 898–910 (2005).
74. S. Moussaoui et al., "Separation of non-negative mixture of non-negative sources using a Bayesian approach and MCMC sampling," *IEEE Trans. Signal Process.* **54**(11), 4133–4145 (2006).
75. T.-H. Chan et al., "A convex analysis-based minimum-volume enclosing simplex algorithm for hyperspectral unmixing," *IEEE Trans. Signal Process.* **57**(11), 4418–4432 (2009).
76. J.-P. Combe et al., "Analysis of OMEGA/Mars Express data hyperspectral data using a Multiple-Endmember Linear Spectral Unmixing Model (MELSUM): methodology and first results," *Planet. Space Sci.* **56**(7), 951–975 (2008).
77. X. Ceamanos et al., "Intercomparison and validation of techniques for spectral unmixing of hyperspectral images: a planetary case study," *IEEE Trans. Geosci. Remote Sens.* **49**(11), 4341–4358 (2011).
78. A. Brown, "Spectral curve fitting for automatic hyperspectral data analysis," *IEEE Trans. Geosci. Remote Sens.* **44**(6), 1601–1608 (2006).
79. M. A. McCraig et al., "Fitting the curve in Excel®: systematic curve fitting of laboratory and remotely sensed planetary spectra," *Comput. Geosci.* **100**, 103–114 (2017).
80. S. Asadzadeh and C. R. de Souza Filho, "A review on spectral processing methods for geological remote sensing," *Int. J. Appl. Earth Observ. Geoinf.* **47**, 69–90 (2016).
81. R. N. Clark and T. L. Roush, "Reflectance spectroscopy: quantitative analysis techniques for remote sensing applications," *J. Geophys. Res. Solid Earth* **89**(B7), 6329–6340 (1984).
82. R. N. Clark and T. V. King, "Automatic continuum analysis of reflectance spectra," in *JPL Proc. 3rd Airborne Imaging Spectrom. Data Anal. Workshop* (1987).
83. R. N. Clark et al., "Imaging spectroscopy: Earth and planetary remote sensing with the USGS Tetracorder and expert systems," *J. Geophys. Res. Planets* **108**(E12) (2003).
84. P. Kumari et al., "Segmented curve-fitting method for continuum removal in hyperspectral images," Working paper or preprint (2023).
85. H. Zhao et al., "Hyperspectral feature extraction based on the reference spectral background removal method," *IEEE J. Sel. Top. Appl. Earth Observ. Remote Sens.* **8**(6), 2832–2844 (2015).
86. C. Mielke et al., "New geometric hull continuum removal algorithm for automatic absorption band detection from spectroscopic data," *Remote Sens. Lett.* **6**(2), 97–105 (2015).
87. Y. Yang, S. Jin, and Y. Xue, "Identification of minerals at Martian Jezero Crater using MRO CRISM images," in *XXXIth URSI General Assembly and Sci. Symp. (URSI GASS)*, IEEE, pp. 1–4 (2014).
88. E. Allender and T. F. Stepinski, "Automatic, exploratory mineralogical mapping of CRISM imagery using summary product signatures," *Icarus* **281**, 151–161 (2017).
89. A. M. Saranathan and M. Parente, "Adversarial feature learning for improved mineral mapping of CRISM data," *Icarus* **355**, 114107 (2021).
90. B. D. Bue, "An evaluation of low-rank Mahalanobis metric learning techniques for hyperspectral image classification," *IEEE J. Sel. Top. Appl. Earth Observ. Remote Sens.* **7**(4), 1079–1088 (2014).

91. B. D. Bue et al., "Metric learning for hyperspectral image segmentation," in *3rd Workshop on Hyperspectral Image and Signal Process.: Evol. in Remote Sens. (WHISPERS)*, IEEE, pp. 1–4 (2011).
92. X. Wu et al., "Joint Hapke model and spatial adaptive sparse representation with iterative background purification for Martian serpentine detection," *Remote Sens.* **13**(3), 500 (2021).
93. X. Wu et al., "Imaging Mars analog minerals' reflectance spectra and testing mineral detection algorithms," *Icarus* **369**, 114644 (2021).
94. M. Dundar and B. L. Ehlmann, "Rare jarosite detection in CRISM imagery by non-parametric Bayesian clustering," in *8th Workshop on Hyperspectral Image and Signal Process.: Evol. in Remote Sens. (WHISPERS)*, IEEE, pp. 1–5 (2016).
95. E. Plebani et al., "A machine learning toolkit for CRISM image analysis," *Icarus* **376**, 114849 (2022).
96. H. Z. Yerebakan, B. Rajwa, and M. Dundar, "The infinite mixture of infinite Gaussian mixtures," in *Adv. in Neural Inf. Process. Syst.*, Vol. **27** (2014).
97. M. Dundar, L. Li, and B. Rajwa, "Partially-observed models for classifying minerals on Mars," in *5th Workshop on Hyperspectral Image and Signal Process.: Evol. in Remote Sens. (WHISPERS)*, IEEE, pp. 1–4 (2013).
98. D. R. Thompson et al., "Superpixel endmember detection," *IEEE Trans. Geosci. Remote Sens.* **48**(11), 4023–4033 (2010).
99. J. Caggiano et al., "Application of machine learning to identify surface minerals in CRISM imagery," *Lunar Planet. Sci.* **50** (2019).
100. P.-E. Danielsson, "Euclidean distance mapping," *Comput. Graph. Image Process.* **14**(3), 227–248 (1980).
101. G. J. McLachlan, "Mahalanobis distance," *Resonance* **4**(6), 20–26 (1999).
102. F. A. Kruse et al., "The spectral image processing system (SIPS)—interactive visualization and analysis of imaging spectrometer data," *Remote Sens. Environ.* **44**(2–3), 145–163 (1993).
103. G. Turin, "An introduction to matched filters," *IRE Trans. Inf. Theory* **6**(3), 311–329 (1960).
104. D. A. Reynolds et al., "Gaussian mixture models," in *Encyclopedia of Biometrics*, Vol. **741**, pp. 659–663, Springer, Berlin (2009).
105. C. Wang, J. Paisley, and D. M. Blei, "Online variational inference for the hierarchical Dirichlet process," in *Proc. Fourteenth Int. Conf. on Artif. Intell. and Stat.*, JMLR, pp. 752–760 (2011).
106. G. M. Allenby and P. E. Rossi, "Hierarchical Bayes models," in *The Handbook of Marketing Research: Uses, Misuses, and Future Advances*, pp. 418–440, Elsevier (2006).
107. M. Ankerst et al., "OPTICS: ordering points to identify the clustering structure," *ACM Sigmod Record* **28**(2), 49–60 (1999).
108. K. L. Wagstaff et al., "Guiding scientific discovery with explanations using DEMUD," in *Twenty-Seventh AAAI Conf. on Artif. Intell.* (2013).
109. J. H. Gruninger, A. J. Ratkowski, and M. L. Hoke, "The sequential maximum angle convex cone (SMACC) endmember model," *Proc. SPIE* **5425**, 1–14 (2004).
110. M. E. Winter, "N-FINDR: an algorithm for fast autonomous spectral end-member determination in hyperspectral data," *Proc. SPIE* **3753**, 266–275 (1999).
111. V. K. Ojha, A. Abraham, and V. Snášel, "Metaheuristic design of feedforward neural networks: a review of two decades of research," *Eng. Appl. Artif. Intell.* **60**, 97–116 (2017).
112. Y. LeCun, Y. Bengio, and G. Hinton, "Deep learning," *Nature* **521**(7553), 436–444 (2015).
113. A. Saranathan and M. Parente, "Active classification of neutral spectra for CRISM images," in *48th Annu. Lunar and Planet. Sci. Conf.*, No. 1964, p. 2866 (2017).

Priyanka Kumari is a senior research fellow in the Department of Water Resources and Ocean Engineering at the National Institute of Technology, Karnataka (NITK). She received her BTech degree in electrical and electronics engineering in 2013 from BPUT, Rourkela. She received her MTech degree in remote sensing in 2015 from BIT Mesra, Ranchi. Her research interests include remote sensing, geographic information systems, and machine learning.

Sampriti Soor received his BTech degree in information technology from West Bengal University of Technology in 2011, followed by an ME degree in software engineering from Jadavpur University, Kolkata, in 2015. He received his PhD in computer science from the Indian Statistical Institute in 2022. Currently, he serves as an assistant professor at Kalinga Institute of Industrial Technology, Bhubaneswar. His research focuses on remote sensing, image processing, and mathematical morphology.

Amba Shetty received her bachelor's degree in civil engineering and master's degree in hydraulics and water resources engineering from the NITK, India. She has received her PhD from NITK in 2006. Currently, she is a professor in the Department of Water Resources and Ocean

Engineering at NITK. Her research interests include hydrological modeling, hyperspectral remote sensing, GIS, surface water hydrology, and flood studies.

Shashidhar G. Koolagudi recieved his bachelor's degree in computer science and engineering from Karnataka University, Dharwad, India, and his master's degree in computer science and information technology from the Indian Institute of Engineering Science and Technology, Shibpur, Howrah. He received his PhD from Indian Institute of Technology, Kharagpur, in 2011. His research interests includes machine learning, speech, and audio signal processing. He currently serves as an associate professor at NITK, Surathkal, India.